Journal Title
XX(X):1–20
DOI: 10.1177/ToBeAssigned
www.sagepub.com/
SAGE

A transformable tethered aerial platform for robot-environment interactions

Ruobing Wang[1], Songnan Bai[2], Kaixu Dong[3], Hongqiang Wang[4] and Pakpong Chirarattananon[5]

Abstract

Improving the adaptability and versatility of micro aerial robots is crucial for expanding their application range. In this paper, we present a transformable tethered aerial platform composed of two bicopters tethered together with a cable, which is capable of mid-air transitions and robot-environment physical interactions. The platform can operate in three modes: free-flight mode, tethered-flight mode, and quadcopter mode. These modes are enabled by changing the tension and length of the cable, without the need for additional reconfiguration mechanisms. To fully exploit the capabilities of the proposed system, we derive the dynamic model of the platform and develop the control methods for each mode. The developed controller ensures stable flight in each mode and also enables the platform to operate with limited position feedback. We validate the feasibility of the transformable design through a series of experiments, demonstrating stable transitions between modes and effective physical interactions. Notably, by using the cable as an end effector, the platform can exert forces and torques on the environment through cable tension, eliminating the need for extra grippers or actuators and showcasing the versatility of the system in real-world tasks.

Keywords

Aerial robotics, dynamics, motion control, reconfiguration, robot-environment physical interaction

1 Introduction

Micro aerial robots have garnered significant attention in recent years due to their potential for a wide range of applications, including search and rescue (Schedl et al. 2021), environmental monitoring (Aucone et al. 2023), infrastructure inspection (Lee et al. 2023), precision agriculture (Pretto et al. 2020), and aerial photography (Xiao et al. 2022). Their small size, maneuverability, and ability to access hard-to-reach locations and provide aerial perspectives have driven significant research interests and commercial deployments (Floreano and Wood 2015). However, as applications continue to diversify, the need for adaptable aerial platforms that can operate effectively in varied environments and perform multiple tasks becomes increasingly apparent. Traditional aerial robots face fundamental limitations when required to adapt to changing environments or engage in physical interactions.

Existing micro aerial robots can be broadly categorized into fixed-configuration platforms and reconfigurable systems. Fixed-configuration designs, such as conventional quadcopters (Mellinger et al. 2012), offer high agility but are fundamentally underactuated. More recent fixed designs include fully-actuated multirotor platforms featuring fixedly-tilted propellers (Michieletto et al. 2018; Brescianini and D'Andrea 2018; Park et al. 2018), which enable omnidirectional wrench generation for aerial manipulation tasks without changing their geometric structure (Ryll et al. 2019). While these fully-actuated systems enhance physical interaction capabilities, they typically suffer from reduced flight efficiency and payload capacity due to thrust losses from non-vertical propeller orientations. Reconfigurable systems, on the other hand, offer adaptability to different operational requirements. These include morphing structures that change geometry during flight—from quadrotors with variable rotor tilting mechanisms (Zheng et al. 2020; Liu et al. 2024; Tang and Mueller 2025) to foldable designs that can navigate confined spaces (Riviere et al. 2018; Falanga et al. 2018; Bucki et al. 2023; Jia et al. 2023b). Modular approaches (Bai and Chirarattananon 2022; Jia et al. 2023a; Li et al. 2023) allow robots to reconfigure by connecting and disconnecting individual units, though they require complex docking mechanisms and precise alignment.

An emerging alternative is the use of tethered aerial systems. While cables and tethers have originally been used with a single robot for power supply (Choi et al. 2014), data transmission (Gu et al. 2016), and stabilization (Lupashin and D'Andrea 2013), researchers have begun exploring the tether itself as a multi-functional element due to their light

[1]Department of Construction and Quality Management, Hong Kong Metropolitan University, Hong Kong SAR, China
[2]Department of Civil Engineering, The University of Hong Kong, Hong Kong SAR, China
[3]Department of Biomedical Engineering, City University of Hong Kong, Hong Kong SAR, China
[4]Department of Mechanical and Energy Engineering, Southern University of Science and Technology, Shenzhen, China
[5]Department of Mechanical and Industrial Engineering, University of Toronto, Toronto, Canada

Corresponding author:
Pakpong Chirarattananon, Department of Mechanical and Industrial Engineering, University of Toronto, Toronto, ON M5S 3G8, Canada.
Email: p.chirarattananon@utoronto.ca

weight, low cost, and simple design requirements. Single-tethered aerial robots have demonstrated capabilities for forceful manipulation (Estrada et al. 2018), construction of tensile structures (Augugliaro et al. 2013), perching in cluttered environments (Zhang et al. 2017), and even physically guiding humans (Tognon et al. 2021). Inspired by cable-driven parallel robots (Cheng and Lau 2023), catenary robots—formed by two or more quadcopters connected via a cable—have demonstrated the ability to carry payload (Dong et al. 2023), control cable shape (D'antonio et al. 2021), tie cable hitches (D'Antonio et al. 2023), and perform non-prehensile manipulation tasks (Cardona et al. 2021).

While both reconfigurable aerial robots and tethered aerial systems offer adaptability, they each have significant limitations. Reconfigurable platforms typically require additional dedicated end effectors to perform meaningful physical interactions, increasing weight and complexity (Allenspach et al. 2020; Bodie et al. 2020; Nguyen and Alexis 2021; Cuniato et al. 2023). Existing multi-robot tethered approaches primarily focus on cooperative object manipulation rather than direct environmental interaction using the tether (Gassner et al. 2017; Sanalitro et al. 2020; Dong et al. 2023; Li et al. 2025). Moreover, these systems generally retain a spatially distributed multi-vehicle configuration throughout operation. While such configurations are well suited to cooperative manipulation, their geometric footprint and mechanical topology cannot be substantially altered to accommodate different access and interaction requirements (Sun et al. 2025).

To address these challenges, we propose a transformable tethered aerial platform designed for access-then-interact missions that can switch between three reversible modes (Figure 1 and Supplementary Video). The platform consists of two cable-connected bicopters that can (i) fly independently with a slack tether (free-flight mode), (ii) coordinate to tension the cable for interaction (tethered-flight mode), or (iii) reel in the cable and dock to form a single compact quadcopter for traversal through cluttered or confined spaces (quadcopter mode). Compared with single-configuration aerial manipulators, our approach enables cable-based physical interaction without adding end effectors. Compared with conventional multi-robot tethered systems (Dong et al. 2023; Li et al. 2025; Sun et al. 2025), the transformable architecture allows the same platform to switch between spatially distributed and compact configurations, adapting its geometric footprint and interaction capability to different stages of an access-then-interact mission.

In free-flight mode, the two bicopters fly independently with the cable remaining slack, resulting in minimal coupled dynamics between the two bicopters. Each bicopter has independent flight control, allowing it to navigate separately within cable range. In tethered-flight mode, the bicopters tilt their thrust directions to create tension in the cable, constraining their relative positions while maintaining a fixed distance determined by the winch on Bicopter 1. This enables the system to perform physical interactions with the environment using the cable as an end effector for tasks such as manipulation, payload transport, and perching. Finally, in quadcopter mode, the cable is reeled in, and the two bicopters form a single rigid system, making it suitable for navigating confined spaces. These mode transitions are fully reversible, enabling the system to adapt to different operational requirements during a single mission. By integrating reconfigurability and tethered interaction within a single compact platform, this work overcomes the limitations of conventional reconfigurable and multi-robot tethered systems, expanding the capabilities of aerial robots for physical interactions. As summarized in Table 1, our platform achieves multiple operating modes and cable-based interaction with low actuation and reconfiguration complexity.

The rest of this paper is organized as follows: Section 2 describes the mechanical structure of the proposed platform and its three operating modes. Section 3 presents the dynamic modeling, including translational and attitude dynamics, considering the equilibrium conditions for the tethered-flight and quadcopter modes. Section 4 details the multi-mode flight control framework, discusses mode transitions, and formulates the physical interaction strategy that enables force exertions and environmental interactions using the cable. Section 5 presents experimental results, validating the platform's capabilities in multi-mode flight, object manipulation, and perching—including both guided perching via cable wrapping and dynamic perching using swing motion. Finally, Section 6 concludes the paper.

2 System overview

The proposed platform consists of two bicopters connected by a tether, as illustrated in Figure 1(a). Each bicopter has two rotors for thrust generation and two servo motors for thrust vectoring. Magnets on the bicopters' undersides enable connection, forming a rotational joint when in proximity. Bicopter 1 (left) incorporates a winch with a geared motor and encoder to adjust cable length, while Bicopter 2 (right) is equipped with a force sensor to measure cable tension.

The proposed platform operates in three modes, as shown in Figure 1(b). It typically takes off in the free-flight mode, where the cable remains slack, allowing the two bicopters to fly independently. To transition to the tethered-flight mode, the two bicopters tilt their thrust directions to tension the cable, and then the winch on Bicopter 1 reels in the cable to constrain the distance between the two bicopters. Finally, when the bicopters are sufficiently close, the magnets on the bottom of each bicopter engage, connecting them and transitioning the system into the quadcopter mode, where the bicopters function as a single rigid system. However, the system internally retains one degree of freedom (DoF), allowing the bicopters to rotate relative to each other about their pitch axes. This residual DoF only disappears when the cable length is reduced to zero, and the two bicopters are in full physical contact. The mode transitions are reversible, enabling the system to switch between modes as needed.

Each mode offers distinct capabilities that map to different field scenarios. In free-flight mode, the independent motion of two bicopters provides a wider coverage, enabling concurrent inspection of two adjacent viewpoints of a structure. In tethered-flight mode, the taut cable stabilizes the system, allowing for tasks such as aerial manipulation, payload pickup/delivery, and physical interaction with the

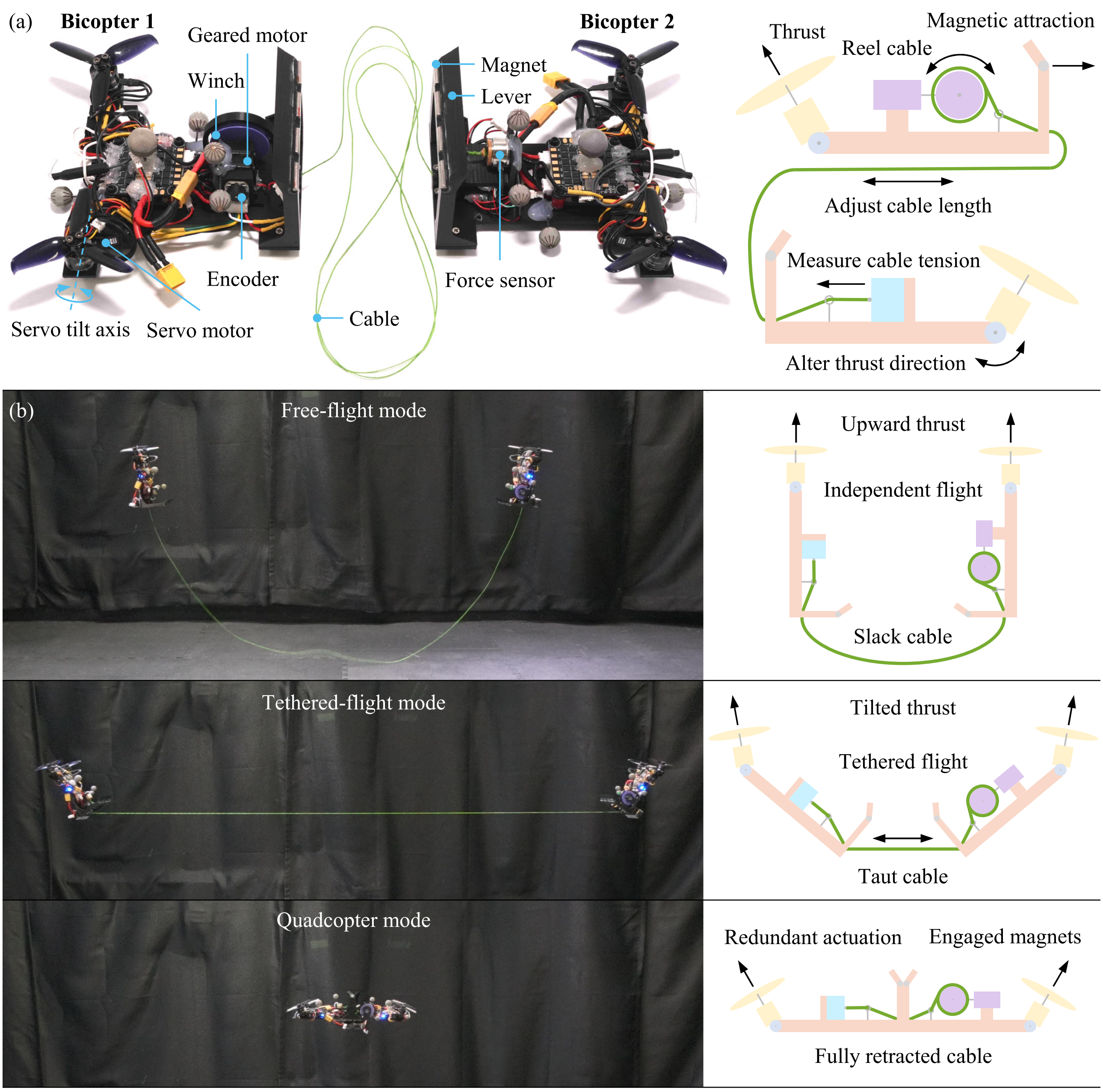

Figure 1. Overview of the proposed platform. (a) Photograph (left) and schematic diagram (right) showing the main components of the platform. (b) Photographs (left) and schematic diagrams (right) demonstrating the three operating modes of the platform.

environment, including structure perching. In quadcopter mode, the system achieves a compact form factor with redundant (tilt-rotor) actuation, making it suitable for navigating narrow spaces or cluttered indoor/industrial spaces before re-expanding for interaction. These capabilities make the proposed platform particularly relevant to real-world applications.

3 Dynamic model

3.1 Preliminaries

In deriving the dynamic model of the proposed platform, we make several simplifying assumptions. The mass and elasticity of the connecting cable are considered negligible. We also disregard the reaction torque caused by the aerodynamic drag on the propellers and the gyroscopic torque generated by changes in the propeller's axis of rotation due to servo actuation. Additionally, the reaction torque arising from the servo motor's angular acceleration is neglected. For clarity, Table 2 lists all variables used in the dynamic model derivation.

The proposed platform consists of two nearly identical bicopters working in tandem. The internal interactions between the bicopters are governed by the cable tension and magnetic forces between the magnets. To simplify the analysis, we derive the attitude dynamics by considering a single tethered bicopter, which represents half of the complete system.

As shown in Figure 2(a), the inertial frame is defined by the unit vectors $\{\boldsymbol{x}_w, \boldsymbol{y}_w, \boldsymbol{z}_w\}$. For Bicopter i where $i \in \{1, 2\}$, the body frame is defined by the unit vectors $\{\boldsymbol{x}_i, \boldsymbol{y}_i, \boldsymbol{z}_i\}$ and is attached to the center of mass (CoM) of the bicopter. The orientation of the body frame relative to the

Table 1. Comparison of the proposed platform with previous works.

Work	Actuation complexity[a]	Structural complexity[b]	End effector type	Modes of operation/configuration	Functional capabilities
This work	Low	Low	Single cable	Free-flight mode, tethered-flight mode, quadcopter mode	Object manipulation, perching, confined space navigation
Ryll et al. (2019)	Medium	Low	Rigid tool	Single flight mode	6D pose control, force exertion
Allenspach et al. (2020)	High	Medium	Rigid tool	Single flight mode	6D pose control, force exertion
Cuniato et al. (2023)	Medium	High	3-DoF manipulator	Single flight mode	Force exertion
Lee et al. (2025)	High	High	4-DoF manipulator	Single flight mode	6D pose control, object manipulation
Jia et al. (2023b)	Low	Medium	None	Flight mode, rolling mode	Confined space navigation
Li et al. (2023)	Low	Low	None	Quadcopter mode, bicopter mode	Confined space navigation
Falanga et al. (2018)	Medium	Medium	Airframe	X configuration, H configuration, O configuration, T configuration	Confined space navigation, object grasping
Bucki et al. (2023)	Low	Medium	Airframe	Unfolded, two-arms folded, four-arms folded	Confined space navigation, perching, object grasping
Jia et al. (2023a)	Low	High	Airframe	Unfolded configuration, folded arm configuration	Perching, 6D pose control, object grasping
Estrada et al. (2018)	Low	Low	Single cable	Single flight mode	Object tugging
D'antonio et al. (2021)	Low	Low	Single cable	Single flight mode	Object transportation
Li et al. (2025)	Low	Medium	Multiple cables	Single flight mode	6D object manipulation
Sun et al. (2025)	Low	Medium	Multiple cables	Single flight mode	6D object manipulation

[a] Actuation complexity is assessed based on the number of independently controlled actuators per individual flightable unit, categorized as low (1–5), medium (6–10), or high ($>$10).
[b] Structural complexity accounts for the mechanical components, joints, reconfiguration mechanisms, and number of cooperating modules, and is qualitatively categorized as low, medium, or high based on overall mechanical and architectural complexity.

Table 2. List of variables used in the dynamic model.

Variables	Definition	Category
$\boldsymbol{x}_w, \boldsymbol{y}_w, \boldsymbol{z}_w$	Primary axes of inertial frame	Constant
$\boldsymbol{x}_i, \boldsymbol{y}_i, \boldsymbol{z}_i$	Primary axes of body frame of Bicopter i	Derived
$\boldsymbol{R}_i, \gamma_i, \beta_i, \alpha_i$	Rotation matrix and Euler angles (z-y-z rotation sequence) of Bicopter i	Measured
$\boldsymbol{p}_i$	Position of CoM of Bicopter i	Measured
$\boldsymbol{u}_c, \phi, \psi$	Cable direction and elevation and azimuth angles	Derived
$\boldsymbol{u}_\phi, \boldsymbol{u}_\psi$	Changes in cable direction with respect to elevation and azimuth angles	Derived
m_i	Mass of Bicopter i	Constant
$\boldsymbol{g}$	Gravitational acceleration	Constant
$\boldsymbol{f}_{a,i}$	Total thrust of Bicopter i	Controlled
f_c	Cable tension	Measured
f_m	Magnetic force	Derived
$\boldsymbol{p}_c$	Position of CoM of entire system	Derived
l_c	Cable length	Measured
$\boldsymbol{I}_i$	Moment of inertia matrix of Bicoipter i	Constant
$\boldsymbol{\omega}_i$	Angular velocity of Bicopter i	Measured
$\boldsymbol{\tau}_{a,i}$	Actuation torque of Bicopter i	Controlled
$\boldsymbol{\tau}_{c,i}$	Torque generated by cable tension on Bicopter i	Derived
$\boldsymbol{\tau}_{m,i}$	Torque generated by magnetic force on Bicopter i	Derived
$T_{i,1}, T_{i,2}$	Individual propeller thrusts of Bicopter i	Controlled
$\theta_{i,1}, \theta_{i,2}$	Servo tilting angles of Bicopter i	Controlled
h_y, h_z	Offset distance of propellers along $\boldsymbol{y}_i$ and $\boldsymbol{z}_i$ axes	Constant
d_c	Offset distance of cable attachment point along $\boldsymbol{z}_i$ axis	Constant
$\boldsymbol{x}_q, \boldsymbol{y}_q, \boldsymbol{z}_q$	Primary axes of body frame in quadcopter mode	Derived
ζ	Configuration angle in quadcopter mode	Derived
d_m	Offset distance of magnets along $\boldsymbol{x}_i$ axis	Constant
d_l	Length of levers	Constant

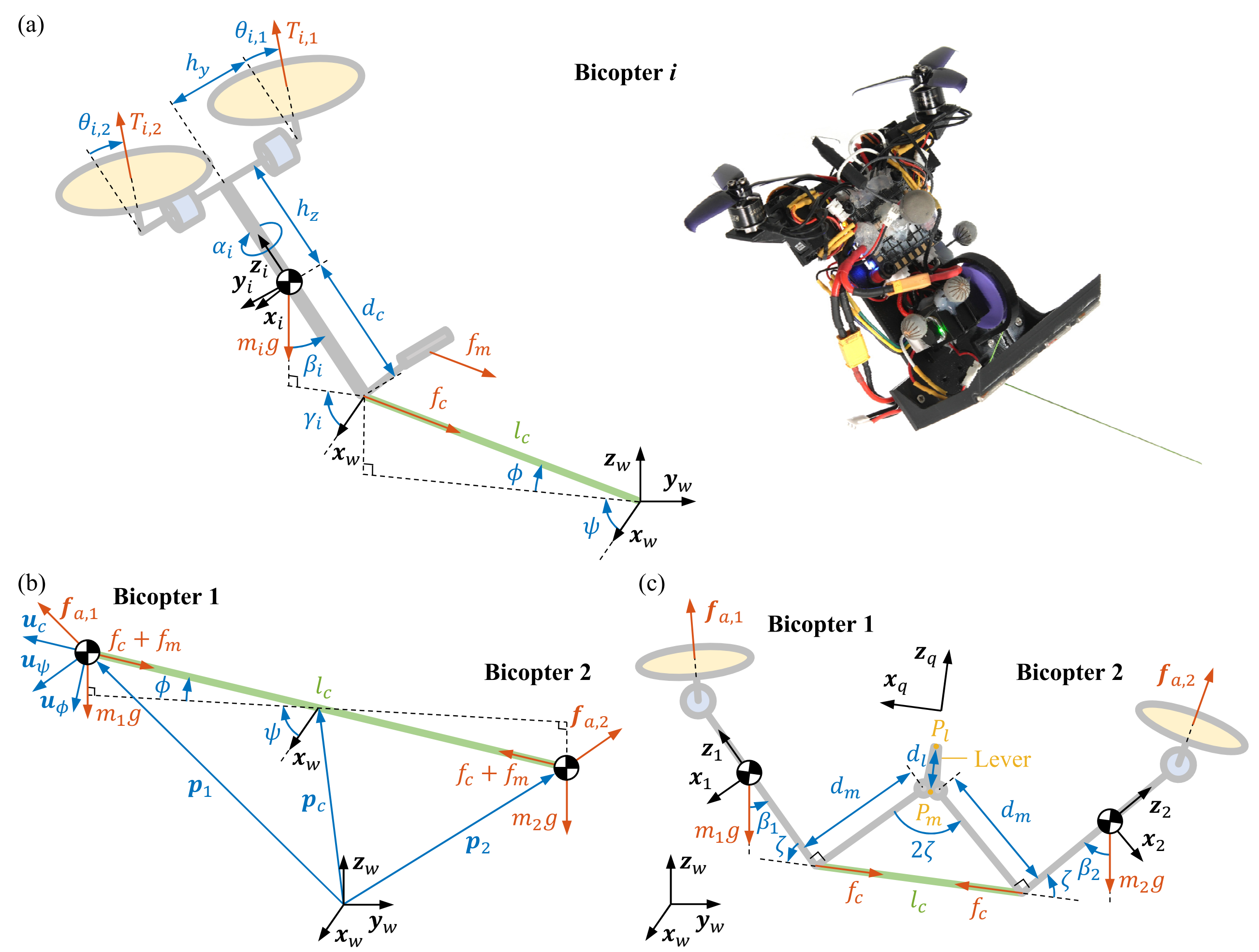

Figure 2. Schematic diagrams of the proposed platform in different operating modes. (a) Half of the system in the tethered flight mode featuring a single bicopter and the cable. (b) The interactions between the two bicopters in the tethered flight mode. (c) The platform in quadcopter mode.

inertial frame is defined by the rotation matrix $\boldsymbol{R}_i$, which is parameterized by the Euler angles (γ_i, β_i, and α_i) following the z-y-z rotation sequence as:

$$\boldsymbol{R}_i = \tag{1}$$

$$\begin{bmatrix} \mathrm{c}\alpha_i\,\mathrm{c}\beta_i\,\mathrm{c}\gamma_i - \mathrm{s}\alpha_i\,\mathrm{s}\gamma_i & -\mathrm{s}\alpha_i\,\mathrm{c}\beta_i\,\mathrm{c}\gamma_i - \mathrm{c}\alpha_i\,\mathrm{s}\gamma_i & \mathrm{s}\beta_i\,\mathrm{c}\gamma_i \\ \mathrm{c}\alpha_i\,\mathrm{c}\beta_i\,\mathrm{s}\gamma_i + \mathrm{s}\alpha_i\,\mathrm{c}\gamma_i & -\mathrm{s}\alpha_i\,\mathrm{c}\beta_i\,\mathrm{s}\gamma_i + \mathrm{c}\alpha_i\,\mathrm{c}\gamma_i & \mathrm{s}\beta_i\,\mathrm{s}\gamma_i \\ -\mathrm{c}\alpha_i\,\mathrm{s}\beta_i & \mathrm{s}\alpha_i\,\mathrm{s}\beta_i & \mathrm{c}\beta_i \end{bmatrix},$$

where s and c are shorthands for sine and cosine functions. The position of the CoM of Bicopter i in the inertial frame is denoted by $\boldsymbol{p}_i = [x_i, y_i, z_i]^\top$.

When the cable is taut, we define:

$$\boldsymbol{u}_c = \begin{bmatrix} \cos\phi\cos\psi & \cos\phi\sin\psi & -\sin\phi \end{bmatrix}^\top, \tag{2}$$

as the unit vector representing the cable direction (from Bicopter 2 to Bicopter 1) in the inertial frame. Here, ϕ and ψ are the elevation and azimuth angles as the cable direction is a unit vector constrained to the 2-sphere S^2, unlike a full rotation, which evolves on $SO(3)$. The change in the cable direction can be captured by the following two vectors:

$$\boldsymbol{u}_\phi = \frac{\partial \boldsymbol{u}_c}{\partial \phi} = \begin{bmatrix} -\sin\phi\cos\psi & -\sin\phi\sin\psi & -\cos\phi \end{bmatrix}^\top, \tag{3}$$

$$\boldsymbol{u}_\psi = \frac{\partial \boldsymbol{u}_c}{\partial \psi} = \begin{bmatrix} -\cos\phi\sin\psi & \cos\phi\cos\psi & 0 \end{bmatrix}^\top. \tag{4}$$

Given the design parameters of the system, $\boldsymbol{u}_c$ can be computed directly from the states ($\boldsymbol{p}_i, \boldsymbol{R}_i$) of the bicopters.

3.2 Translational dynamics

To simplify the derivation of the translational dynamics, the system is modeled as two point masses connected by a cable, as shown in Figure 2(b). For Bicopter i, $\boldsymbol{p}_i$ and $\boldsymbol{f}_{a,i}$ represent the position vector and thrust vector in the inertial frame, respectively. Applying Newton's second law to each bicopter yields:

$$m_i \ddot{\boldsymbol{p}}_i = m_i \boldsymbol{g} + \boldsymbol{f}_{a,i} + (-1)^i (f_c + f_m) \boldsymbol{u}_c, \tag{5}$$

where m_i is the mass of the bicopter, $\boldsymbol{g} = [0, 0, -g]^\top$ is the gravitational acceleration, f_c is the cable tension, and f_m is the magnetic force. Both f_c and f_m act along $\boldsymbol{u}_c$ and are mode-dependent. In the free-flight mode, $f_c = 0$ because the cable is slack. In contrast, $f_c > 0$ in both the tethered-flight and quadcopter modes. The magnetic force between the bicopters f_m exhibits a quadratic decay with distance and is negligible except when the platform operates in the quadcopter mode, where the magnets are in close proximity.

Summing (5) for $i = 1$ and 2 gives the motion of the system's CoM:

$$\ddot{\boldsymbol{p}}_c = \frac{m_1\ddot{\boldsymbol{p}}_1 + m_2\ddot{\boldsymbol{p}}_2}{m_1 + m_2} = \boldsymbol{g} + \frac{\boldsymbol{f}_{a,1} + \boldsymbol{f}_{a,2}}{m_1 + m_2}. \tag{6}$$

When the cable of length l_c is taut, the relative position between the two bicopters depends on $\boldsymbol{u}_c$ as:

$$\boldsymbol{p}_1 - \boldsymbol{p}_2 = l_c\boldsymbol{u}_c. \tag{7}$$

Assuming l_c varies slowly compared with the positions of the bicopters ($\dot{l}_c = 0$), we obtain the relative velocity and acceleration:

$$\dot{\boldsymbol{p}}_1 - \dot{\boldsymbol{p}}_2 = l_c(\boldsymbol{u}_\phi\dot{\phi} + \boldsymbol{u}_\psi\dot{\psi}), \tag{8}$$

$$\ddot{\boldsymbol{p}}_1 - \ddot{\boldsymbol{p}}_2 = l_c(\boldsymbol{u}_\phi\ddot{\phi} + \boldsymbol{u}_\psi\ddot{\psi} + \dot{\boldsymbol{u}}_\phi\dot{\phi} + \dot{\boldsymbol{u}}_\psi\dot{\psi}), \tag{9}$$

where $\dot{\boldsymbol{u}}_\phi\dot{\phi}$ and $\dot{\boldsymbol{u}}_\psi\dot{\psi}$ are Coriolis and centrifugal terms, which can be neglected for non-aggressive maneuvers. Projecting the result along $\boldsymbol{u}_\phi$ and $\boldsymbol{u}_\psi$ yields:

$$\ddot{\phi} = \frac{(\ddot{\boldsymbol{p}}_1 - \ddot{\boldsymbol{p}}_2)^\top\boldsymbol{u}_\phi}{l_c},\ \ddot{\psi} = \frac{(\ddot{\boldsymbol{p}}_1 - \ddot{\boldsymbol{p}}_2)^\top\boldsymbol{u}_\psi}{l_c\cos^2\phi}. \tag{10}$$

Finally, substituting $\ddot{\boldsymbol{p}}_i$ from (5) into (10), we obtain:

$$\ddot{\phi} = \left(\frac{\boldsymbol{f}_{a,1}}{m_1} - \frac{\boldsymbol{f}_{a,2}}{m_2}\right)^\top\frac{\boldsymbol{u}_\phi}{l_c}, \tag{11}$$

$$\ddot{\psi} = \left(\frac{\boldsymbol{f}_{a,1}}{m_1} - \frac{\boldsymbol{f}_{a,2}}{m_2}\right)^\top\frac{\boldsymbol{u}_\psi}{l_c\cos^2\phi}. \tag{12}$$

Together, (6), (11), and (12) describe the translational dynamics, capturing both the CoM motion and the relative positions through elevation and azimuth angles.

3.3 Attitude dynamics

Using Euler's equation, the attitude dynamics of the tethered bicopter in the body frame is derived as:

$$\boldsymbol{I}_i\dot{\boldsymbol{\omega}}_i + \boldsymbol{\omega}_i \times \boldsymbol{I}_i\boldsymbol{\omega}_i = \boldsymbol{\tau}_{a,i} + \boldsymbol{\tau}_{c,i} + \boldsymbol{\tau}_{m,i}, \tag{13}$$

where $\boldsymbol{I}_i$ is the moment of inertia matrix, $\boldsymbol{\omega}_i$ is the angular velocity vector, $\boldsymbol{\tau}_{a,i}$ is the actuation torque vector generated by the propeller thrusts, $\boldsymbol{\tau}_{c,i}$ is the torque vector generated by the cable tension, and $\boldsymbol{\tau}_{m,i}$ is the torque vector generated by the magnetic force, all represented in the body frame.

The bicopter uses the differential propeller thrusts to generate the actuation torque in the $\boldsymbol{x}_i$ direction (roll). The actuation torques in the $\boldsymbol{y}_i$ and $\boldsymbol{z}_i$ directions (pitch and yaw) are produced by the two servo motors that tilt the propellers in the same and opposite directions, respectively.

According to the geometric relations described in Figure 2(a), the actuation torque $\boldsymbol{\tau}_{a,i}$ is expressed as:

$$\boldsymbol{\tau}_{a,i} = \begin{bmatrix}\tau_{a,i}^{(x)}\\ \tau_{a,i}^{(y)}\\ \tau_{a,i}^{(z)}\end{bmatrix} = \begin{bmatrix}-T_{i,1}\cos\theta_{i,1}h_y + T_{i,2}\cos\theta_{i,2}h_y\\ T_{i,1}\sin\theta_{i,1}h_z + T_{i,2}\sin\theta_{i,2}h_z\\ T_{i,1}\sin\theta_{i,1}h_y - T_{i,2}\sin\theta_{i,2}h_y\end{bmatrix}, \tag{14}$$

where $T_{i,1}$ and $T_{i,2}$ are the thrust forces generated by the propellers, $\theta_{i,1}$ and $\theta_{i,2}$ are the propeller tilting angles controlled by the servo motors, and h_y and h_z are the offset distances of the propellers along the $\boldsymbol{y}_i$ and $\boldsymbol{z}_i$ axes of the body frame.

The cable, attached to the bottom of the bicopter, generates a torque $\boldsymbol{\tau}_{c,i}$ given by:

$$\boldsymbol{\tau}_{c,i} = \begin{bmatrix}\tau_{c,i}^{(x)}\\ \tau_{c,i}^{(y)}\\ 0\end{bmatrix} = \begin{bmatrix}0\\ 0\\ -d_c\end{bmatrix} \times (-1)^i f_c\boldsymbol{R}_i^\top\boldsymbol{u}_c, \tag{15}$$

where d_c is the offset distance of the cable attachment point along the $\boldsymbol{z}_i$ axis of the body frame. Unlike common simplifying assumptions that place the tether attachment at the CoM (Sanalitro et al. 2020; Dong et al. 2023; Li et al. 2025), the nonzero offset d_c induces a cable-tension moment that couples attitude and cable-direction dynamics, which must be compensated for by the controller.

Similar to f_m, $\boldsymbol{\tau}_{m,i}$ is negligible in the free-flight and tethered-flight modes. Its role is only to construct a rotational joint formed in the quadcopter mode.

3.4 Tethered flight in static equilibrium

To keep the model tractable for control, we simplify the dynamics for the tethered-flight mode. In static equilibrium, the forces on Bicopter i (propeller thrust, gravity, and cable tension) are balanced. Equation (5) becomes:

$$m_i\boldsymbol{g} + \boldsymbol{f}_{a,i} + (-1)^i f_c\boldsymbol{u}_c = \boldsymbol{0}. \tag{16}$$

The thrust vector can be expressed as $\boldsymbol{f}_{a,i} = \boldsymbol{R}_i\boldsymbol{T}_{a,i}$, where $\boldsymbol{T}_{a,i}$ is the thrust vector in the body frame given as a function of actuation commands. Since the rotational axis of the servos is along $\boldsymbol{y}_i$, $\boldsymbol{T}_{a,i}$ lies exclusively in the $\boldsymbol{x}_i$-$\boldsymbol{z}_i$ plane:

$$\boldsymbol{T}_{a,i} = \begin{bmatrix}\tau_{a,i}^{(y)}/h_z\\ 0\\ T_{a,i}^{(z)}\end{bmatrix} = \begin{bmatrix}T_{i,1}\sin\theta_{i,1} + T_{i,2}\sin\theta_{i,2}\\ 0\\ T_{i,1}\cos\theta_{i,1} + T_{i,2}\cos\theta_{i,2}\end{bmatrix}. \tag{17}$$

For (16) to hold, all the forces must be coplanar, lying on the $\boldsymbol{x}_i$-$\boldsymbol{z}_i$ plane in static equilibrium. This condition imposes constraints on the Euler angles: $\alpha_i = 0$ and $\gamma_i = \psi + (i - 1)\pi$. Applying these constraints to (13) and (16), we derive the equilibrium conditions:

$$T_{a,i}^{(z)} = \frac{m_i g}{h_z + d_c}\Big(h_z\cos\phi\sec\left(\beta_i + (-1)^i\phi\right) + d_c\cos\beta_i\Big), \tag{18}$$

$$\tau_{a,i}^{(x)} = 0,\ \tau_{a,i}^{(y)} = -\frac{m_i g}{h_z + d_c}h_z d_c\sin\beta_i,\ \tau_{a,}^{(z)} = 0, \tag{19}$$

$$f_c = \frac{m_i g}{h_z + d_c}h_z\sin\beta_i\sec\left(\beta_i + (-1)^i\phi\right). \tag{20}$$

In particular, (19) states that a non-zero pitch torque, produced by tilted propellers as shown in (17), is needed for the bicopter to stay in equilibrium. This is to counter the torque produced by the cable. These conditions serve as feedforward terms for control, compensating for cable-tension-induced force and torque.

3.5 Quadcopter configuration

In the quadcopter mode (Figure 2(c)), the magnets connect the two bicopters, forming a rotational joint at point P_m.

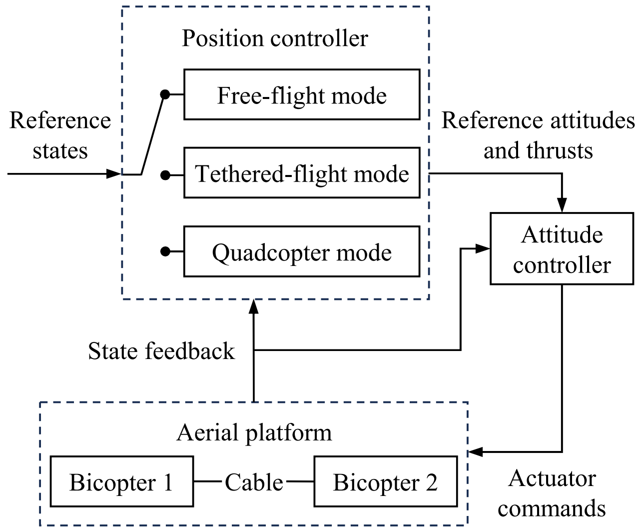

Figure 3. Block diagram of the multi-mode flight control. The controller follows a hierarchical structure: the position controller is mode-dependent, while the attitude controller remains consistent across all modes, stabilizing each bicopter by tracking reference orientations and thrust commands.

The joint axis is aligned with $\boldsymbol{y}_1$ and $\boldsymbol{y}_2$. The magnetic force constrains their relative attitude, but still leaving one rotational DoF between the two bicopters. To describe the system's orientation in this mode, we introduce an additional frame defined by unit vectors $\{\boldsymbol{x}_q, \boldsymbol{y}_q, \boldsymbol{z}_q\}$:

$$\boldsymbol{x}_q = \frac{\boldsymbol{z}_1 - \boldsymbol{z}_2}{\|\boldsymbol{z}_1 - \boldsymbol{z}_2\|},\ \boldsymbol{y}_q = \boldsymbol{y}_1 = -\boldsymbol{y}_2,\ \boldsymbol{z}_q = \boldsymbol{x}_q \times \boldsymbol{y}_q. \quad (21)$$

The relative angle between the two bicopters in this mode, denoted by 2ζ (Figure 2(c)), is determined by the cable length l_c according to:

$$2\zeta = \pi - \beta_1 - \beta_2 = 2 \arcsin\left(\frac{l_c}{2d_m}\right), \quad (22)$$

where d_m is the offset distance of the magnets along the $\boldsymbol{x}_i$ axis of each body frame.

4 Multi-mode flight control

As shown in Figure 3, the control framework for the proposed platform adopts a cascaded structure, similar to how conventional quadcopters are typically controlled (Mellinger et al. 2012), comprising a position controller and an attitude controller. The attitude controller operates at the lower level, ensuring that (i) the attitude of each bicopter and (ii) the thrust along its main axis ($\boldsymbol{z}_i$) follow the setpoints generated by the position controller. This setup is consistent across all operating modes. However, unlike a regular quadcopter, the thrust direction of a bicopter in its body frame is not fixed, meaning the thrust setpoint only refers to the principal component, while lateral components ($\boldsymbol{x}_i$ and $\boldsymbol{y}_i$) are ignored, similar to the approach in Qin et al. (2020).

The position controller, on the other hand, is tailored for each of the platform's operating modes. In free-flight mode, the controllers on both bicopters function independently. Position setpoints are predetermined to maintain the bicopters sufficiently close, ensuring the cable remains slack and can be neglected in the control calculations. In tethered-flight mode, the position controller incorporates feedforward terms to maintain cable tension, while simultaneously regulating the CoM position of the entire system and aligning the cable direction with the desired orientation. Finally, in quadcopter mode, where the system configuration is still influenced by the cable length, the position controller is similar to that used in tethered-flight mode but omits control of the cable direction. Instead, it accounts for the coupling between the relative attitude of the two bicopters and the cable length.

The following subsections detail the design of the attitude controller, followed by the position controller for each operating mode. Additionally, we outline the mode transition strategy and discuss how the platform interacts with external objects. An overall analysis of the stability and robustness of the proposed multi-mode flight control is provided in the Supplementary Materials.

4.1 Attitude control

For Bicopter i, the goal is to track a reference rotation matrix $\boldsymbol{R}_{r,i}$ and an axial thrust reference $T_{r,i}^{(z)}$ provided by the position controller. The actuation torque $\boldsymbol{\tau}_{a,i}$ is computed using a proportional-derivative (PD) controller (Yu et al. 2015):

$$\boldsymbol{\tau}_{a,i} = \boldsymbol{K}_{a,p}\left(\log(\boldsymbol{R}_i^\top \boldsymbol{R}_{r,i})\right)^\vee + \boldsymbol{K}_{a,d}(\boldsymbol{\omega}_{r,i} - \boldsymbol{\omega}_i) + \boldsymbol{\tau}_{f,i}, \quad (23)$$

where $\boldsymbol{K}_{a,p}$ and $\boldsymbol{K}_{a,d}$ are positive definite gain matrices, $\boldsymbol{\tau}_{f,i} = [0, \tau_{f,i}^{(y)}, 0]^\top$ is the feedforward torque, $\log(\cdot)$ represents the matrix logarithm function, and $(\cdot)^\vee$ converts a skew-symmetric matrix to a vector. The proportional and derivative terms follow the form introduced in Yu et al. (2015). Here, $\boldsymbol{\omega}_{r,i}$ is calculated from the difference between the reference attitude in the current and previous steps. Depending on the mode of operation, the feedforward torque is added to deal with the cable tension or other interactions.

Once the thrust reference $T_{r,i}^{(z)}$ and actuation torque $\boldsymbol{\tau}_{a,i}$ are determined, the actuator commands (i.e., individual propeller thrusts and servo tilting angles) are computed by inverting the actuation map derived from (14) and the last row of (17):

$$T_{i,1} = \frac{1}{2}\sqrt{\left(\frac{\tau_{a,i}^{(y)}}{h_z} + \frac{\tau_{a,i}^{(z)}}{h_y}\right)^2 + \left(T_{r,i}^{(z)} - \frac{\tau_{a,i}^{(x)}}{h_y}\right)^2}, \quad (24)$$

$$T_{i,2} = \frac{1}{2}\sqrt{\left(\frac{\tau_{a,i}^{(y)}}{h_z} - \frac{\tau_{a,i}^{(z)}}{h_y}\right)^2 + \left(T_{r,i}^{(z)} + \frac{\tau_{a,i}^{(x)}}{h_y}\right)^2}, \quad (25)$$

$$\theta_{i,1} = \arctan\left(\frac{\tau_{a,i}^{(y)} h_y + \tau_{a,i}^{(z)} h_z}{(T_{r,i}^{(z)} h_y - \tau_{a,i}^{(x)}) h_z}\right), \quad (26)$$

$$\theta_{i,2} = \arctan\left(\frac{\tau_{a,i}^{(y)} h_y - \tau_{a,i}^{(z)} h_z}{(T_{r,i}^{(z)} h_y + \tau_{a,i}^{(x)}) h_z}\right). \quad (27)$$

This formulation realizes the desired thrust and torque through propeller forces and servo tilting angles.

4.2 Position control

4.2.1 Free-flight mode. In this mode, the two bicopters operate independently. For Bicopter i, the desired thrust vector $\boldsymbol{f}_{a,i}$ is calculated from the position feedback using a PD controller:

$$\boldsymbol{f}_{a,i} = m_i(\ddot{\boldsymbol{p}}_{r,i} - \boldsymbol{g}) + \boldsymbol{K}_{p,p}(\boldsymbol{p}_{r,i} - \boldsymbol{p}_i) + \boldsymbol{K}_{p,d}(\dot{\boldsymbol{p}}_{r,i} - \dot{\boldsymbol{p}}_i), \tag{28}$$

where $\boldsymbol{p}_{r,i}$ is the reference position, and $\boldsymbol{K}_{p,p}$ and $\boldsymbol{K}_{p,d}$ are positive definite gain matrices.

To determine a reference rotation $\boldsymbol{R}_{r,i} = [\boldsymbol{x}_{r,i}, \boldsymbol{y}_{r,i}, \boldsymbol{z}_{r,i}]$, we assume the thrust vector is primarily aligned with the body frame's $\boldsymbol{z}_i$ axis, which yields:

$$T_{r,i}^{(z)} = \|\boldsymbol{f}_{a,i}\|, \ \boldsymbol{z}_{r,i} = \frac{\boldsymbol{f}_{a,i}}{\|\boldsymbol{f}_{a,i}\|}. \tag{29}$$

Next, we define a heading direction according to a pre-specified yaw angle as a horizontal unit vector: $\boldsymbol{r}_i = [\cos\gamma_{r,i}, \sin\gamma_{r,i}, 0]^\top$. The roll axis $\boldsymbol{x}_{r,i}$ must be coplanar with both $\boldsymbol{z}_{r,i}$ and $\boldsymbol{r}_i$. Therefore:

$$\boldsymbol{x}_{r,i} = \frac{\boldsymbol{r}_i - (\boldsymbol{r}_i^\top \boldsymbol{z}_{r,i})\boldsymbol{z}_{r,i}}{\|\boldsymbol{r}_i - (\boldsymbol{r}_i^\top \boldsymbol{z}_{r,i})\boldsymbol{z}_{r,i}\|}, \ \boldsymbol{y}_{r,i} = \boldsymbol{z}_{r,i} \times \boldsymbol{x}_{r,i}. \tag{30}$$

Moreover, with negligible cable tension and magnetic force, the feedforward torque is not required. That is $\tau_{f,i}^{(y)} = 0$.

4.2.2 Tethered-flight mode. In this mode, the controller regulates the platform's CoM position and cable direction to track reference values $\boldsymbol{p}_{r,c}$, ϕ_r, and ψ_r. The thrust vectors are calculated using three stacked PD controllers:

$$\begin{aligned}\boldsymbol{f}_{a,i} = {} & m_i(\ddot{\boldsymbol{p}}_{r,c} - \boldsymbol{g}) + (-1)^{i-1} f_{r,c}\boldsymbol{u}_c \\ & + \frac{m_i}{m_1 + m_2}\big(\boldsymbol{K}_{p,p}(\boldsymbol{p}_{r,c} - \boldsymbol{p}_c) + \boldsymbol{K}_{p,d}(\dot{\boldsymbol{p}}_{r,c} - \dot{\boldsymbol{p}}_c)\big) \\ & + (-1)^{i-1}\big(K_{\phi,p}(\phi_r - \phi) + K_{\phi,d}(\dot{\phi}_r - \dot{\phi})\big) l_c \boldsymbol{u}_\phi \\ & + (-1)^{i-1}\big(K_{\psi,p}(\psi_r - \psi) + K_{\psi,d}(\dot{\psi}_r - \dot{\psi})\big) l_c \boldsymbol{u}_\psi,\end{aligned} \tag{31}$$

where $f_{r,c}$ is the chosen reference cable tension to prevent slack, and $K_{\phi,p}$, $K_{\phi,d}$, $K_{\psi,p}$, and $K_{\psi,d}$ are positive gains for the cable direction.

To verify the stability of the system's CoM position, notice that the terms related to the cable direction (containing $\boldsymbol{u}_c$, $\boldsymbol{u}_\phi$, and $\boldsymbol{u}_\psi$) cancel out when (31) is substituted into (6), leaving only the terms pertinent to the feedforward acceleration and position errors.

Simultaneously, when the control law in (31) is employed, $\boldsymbol{f}_{a,1}/m_1 - \boldsymbol{f}_{a,2}/m_2$ contains only cable-related components in three orthogonal directions ($\boldsymbol{u}_c$, $\boldsymbol{u}_\phi$, and $\boldsymbol{u}_\psi$). When substituted into (11) and (12), the cable direction is stabilized. In the meantime, the term $(-1)^{i-1} f_{r,c}\boldsymbol{u}_c$ ensures the cable remains taut. Stabilizing the CoM position and cable direction effectively governs the positions of both bicopters due to the kinematic constraint.

The reference rotation matrix $\boldsymbol{R}_{r,i}$ is constructed by considering the influence of the thrust vector on attitude dynamics equilibrium. This begins with the pitch torque equilibrium, assuming the bicopter is in translational equilibrium. We evaluate the total torque—due to weight $m_i\boldsymbol{g}$ and thrust $\boldsymbol{f}_{a,i}$ about the cable attachment point. Both forces act at distances $d_c\boldsymbol{z}_{r,i}$ and $(h_z + d_c)\boldsymbol{z}_{r,i}$, respectively. Projecting this torque along the pitch axis $\boldsymbol{y}_{r,i}$ and equating to zero yields:

$$\begin{aligned}\boldsymbol{y}_{r,i}^\top\Big(\boldsymbol{z}_{r,i} \times \big((h_z + d_c)\boldsymbol{f}_{a,i} + d_c m_i \boldsymbol{g}\big)\Big) &= \\ (\boldsymbol{y}_{r,i} \times \boldsymbol{z}_{r,i})^\top\big((h_z + d_c)\boldsymbol{f}_{a,i} + d_c m_i \boldsymbol{g}\big) &= \\ \boldsymbol{x}_{r,i}^\top\big((h_z + d_c)\boldsymbol{f}_{a,i} + d_c m_i \boldsymbol{g}\big) &= 0,\end{aligned} \tag{32}$$

where we have applied the scalar triple product identity. The outcome directly imposes one constraint on $\boldsymbol{x}_{r,i}$. To fully determine $\boldsymbol{x}_{r,i}$, we opt for $\boldsymbol{x}_{r,i}$ to reside on the vertical $\boldsymbol{u}_c$-$\boldsymbol{u}_\phi$ plane to be consistent with the equilibrium state described in Section 3.4 and Figure 2(a). This is defined by:

$$\boldsymbol{x}_{r,i}^\top \boldsymbol{u}_\psi = 0, \tag{33}$$

as $\boldsymbol{u}_\psi$ is orthogonal to the $\boldsymbol{u}_c$-$\boldsymbol{u}_\phi$ plane. Together, (32) and (33) fully define $\boldsymbol{x}_{r,i}$.

Next, we employ the fact that the thrust vector $\boldsymbol{f}_{a,i}$ must be on the $\boldsymbol{x}_{r,i}$-$\boldsymbol{z}_{r,i}$ plane. This allows us to compute $\boldsymbol{z}_{r,i}$ from $\boldsymbol{f}_{a,i}$ after subtracting component along $\boldsymbol{x}_{r,i}$ as:

$$\boldsymbol{z}_{r,i} = \frac{\boldsymbol{f}_{a,i} - (\boldsymbol{f}_{a,i}^\top \boldsymbol{x}_{r,i})\boldsymbol{x}_{r,i}}{\|\boldsymbol{f}_{a,i} - (\boldsymbol{f}_{a,i}^\top \boldsymbol{x}_{r,i})\boldsymbol{x}_{r,i}\|}. \tag{34}$$

With $\boldsymbol{x}_{r,i}$ and $\boldsymbol{z}_{r,i}$, $\boldsymbol{R}_{r,i}$ is fully determined.

To obtain the axial thrust reference, we take the projection of $\boldsymbol{f}_{a,i}$ along the body axis:

$$T_{r,i}^{(z)} = \boldsymbol{z}_{r,i}^\top \boldsymbol{f}_{a,i}. \tag{35}$$

Lastly, the feedforward pitch torque is obtained by projecting $\boldsymbol{f}_{a,i}$ along $\boldsymbol{x}_{r,i}$:

$$\tau_{f,i}^{(y)} = h_z \boldsymbol{x}_{r,i}^\top \boldsymbol{f}_{a,i} = -\frac{m_i h_z d_c}{h_z + d_c}\boldsymbol{x}_{r,i}^\top \boldsymbol{g}, \tag{36}$$

where we have substituted the expression for $\boldsymbol{x}_{r,i}^\top \boldsymbol{f}_{a,i}$ from (32). Notice that $\tau_{f,i}^{(y)}$ converges to $\tau_{a,i}^{(y)}$ in (19) when the platform reaches static equilibrium (the $\boldsymbol{x}_{r,i}$-$\boldsymbol{z}_{r,i}$ plane coincides with the $\boldsymbol{u}_c$-$\boldsymbol{u}_\phi$ plane).

Moreover, when operating in the tethered-flight mode, the proposed platform retains stability even when only one bicopter receives position feedback. In this configuration, one bicopter is actively regulated by the position controller using feedback from external sensors (e.g., motion capture cameras or global positioning system (GPS)), while the other bicopter relies solely on its onboard attitude controller without explicit position feedback. Under some simplifying assumptions, the stability of this control scheme is validated in the Supplementary Materials. Notably, this property relies on the nonzero tether attachment offset (i.e., $d_c > 0$).

4.2.3 Quadcopter mode. In quadcopter mode, the position control ensures the reference CoM position is tracked, similar to the tethered-flight mode.

Based on the dynamics of the CoM from (6), we reconsider the control law defined by (31). However, since the cable length is short in this mode ($l_c < 2d_m$), we forego the cable-direction-related terms in (31) as they are proportional to l_c. This eliminates the cable direction control effort, resulting in:

$$\boldsymbol{f}_{a,i} = m_i(\ddot{\boldsymbol{p}}_{r,c} - \boldsymbol{g}) + (-1)^{i-1} f_{r,c}\boldsymbol{u}_c + \frac{m_i}{m_1+m_2}\big(\boldsymbol{K}_{p,p}(\boldsymbol{p}_{c,r} - \boldsymbol{p}_c) + \boldsymbol{K}_{p,d}(\dot{\boldsymbol{p}}_{c,r} - \dot{\boldsymbol{p}}_c)\big) + (-1)^{i-1} f_\tau \boldsymbol{z}_w, \quad (37)$$

where the feedforward term $(-1)^{i-1} f_\tau \boldsymbol{z}_w$ is added to satisfy the torque balance condition for the entire quadcopter. Here, the cable direction $\boldsymbol{u}_c$ is directly dictated by the attitude of the bicopters and the cable length through ζ as seen in Figure 2(c).

To evaluate the feedforward term f_τ, we assume the system is in static equilibrium, it can be seen from Figure 2(c) that the entire quadcopter cannot achieve pitch torque balance without this term. As shown in the Supplementary Materials, the torque balance condition is obtained when:

$$f_\tau = \frac{-m_1 g h_z \cos(\phi_r - \zeta) + m_2 g h_z \cos(\phi_r + \zeta)}{2\cos\phi_r\big((h_z + d_c)\cos\zeta + d_m \sin\zeta\big)}, \quad (38)$$

depending on ζ and ϕ_r, irrespective of the attitude reference of each bicopter.

For the attitude setpoints, we first consider the rotation matrix belonging to the entire quadcopter $\boldsymbol{R}_{r,q}$. Thanks to the symmetry and the fact that $\boldsymbol{u}_c$ and $\boldsymbol{f}_{a,i}$ nominally lie in the $\boldsymbol{x}_{r,q}$-$\boldsymbol{z}_{r,q}$ plane of the quadcopter, we first define the reference roll axis $\boldsymbol{x}_{r,q} = \boldsymbol{u}_c$. This leaves $\boldsymbol{z}_{r,q}$ to be the component of $\boldsymbol{f}_{a,1} + \boldsymbol{f}_{a,2}$ perpendicular to $\boldsymbol{x}_{r,q}$ as:

$$\boldsymbol{z}_{r,q} = \frac{(\boldsymbol{f}_{a,1} + \boldsymbol{f}_{a,2}) - \big((\boldsymbol{f}_{a,1} + \boldsymbol{f}_{a,2})^\top \boldsymbol{x}_{r,q}\big)\boldsymbol{x}_{r,q}}{\|(\boldsymbol{f}_{a,1} + \boldsymbol{f}_{a,2}) - \big((\boldsymbol{f}_{a,1} + \boldsymbol{f}_{a,2})^\top \boldsymbol{x}_{r,q}\big)\boldsymbol{x}_{r,q}\|}, \quad (39)$$

allowing $\boldsymbol{R}_{r,q} = [\boldsymbol{x}_{r,q}, \boldsymbol{y}_{r,q}, \boldsymbol{z}_{r,q}]$ to be evaluated as $\boldsymbol{y}_{r,q} = \boldsymbol{z}_{r,q} \times \boldsymbol{x}_{r,q}$.

To compute the resultant attitude reference for each bicopter $\boldsymbol{R}_{r,i}$, we note that $\boldsymbol{x}_{r,i}$ and $\boldsymbol{z}_{r,i}$ of each bicopter also lie in the $\boldsymbol{x}_{r,q}$-$\boldsymbol{z}_{r,q}$ plane (Figure 2(c)). Leveraging the angle 2ζ from (22) and the symmetrical configuration, we define $\boldsymbol{y}_{r,i}$ to be parallel with $\boldsymbol{y}_{r,q}$: $\boldsymbol{y}_{r,i} = (-1)^{i-1}\boldsymbol{y}_{r,q}$. The quadcopter's frame and the bicopter's frame relate through a rotation about $\boldsymbol{y}_{r,q}$ by an angle ζ such that:

$$\boldsymbol{z}_{r,i} = \begin{bmatrix}\boldsymbol{x}_{r,q} & \boldsymbol{z}_{r,q}\end{bmatrix}\begin{bmatrix}\cos\big((-1)^i\zeta + (i-1)\pi\big) \\ -\sin\big((-1)^i\zeta + (i-1)\pi\big)\end{bmatrix}. \quad (40)$$

Then $\boldsymbol{x}_{r,i}$ is given by the right hand rule as $\boldsymbol{x}_{r,i} = \boldsymbol{y}_{r,i} \times \boldsymbol{z}_{r,i}$.

Next, the axial thrust reference is obtained by projecting $\boldsymbol{f}_{a,i}$ along $\boldsymbol{z}_{r,i}$ as:

$$T_{r,i}^{(z)} = \boldsymbol{z}_{r,i}^\top \boldsymbol{f}_{a,i}. \quad (41)$$

The feedforward pitch torque for each bicopter is calculated based on the torque produced by $\boldsymbol{f}_{a,i}$ on each bicopter as:

$$\tau_{f,i}^{(y)} = h_z \boldsymbol{x}_{r,i}^\top \boldsymbol{f}_{a,i}. \quad (42)$$

Similar to other modes, the reference rotation, axial thrust reference, and feedforward pitch torque serve as inputs for the attitude controller for each bicopter to compute the commands for the servos and motors as described above.

4.3 Transitions between flight modes

The transitions between the free-flight and tethered-flight modes are directly achieved by switching between the position controllers in Section 4.2.1 and Section 4.2.2. To ensure a safe and smooth transition, the reference states at the controller switching instant should be carefully designed, as detailed in the Supplementary Materials.

The transition from tethered-flight to quadcopter mode is initiated by reeling in the cable via the winch on Bicopter 1, reducing the inter-bicopter distance. The attachment occurs when the cable length l_c shortens to a threshold value, depending on the reference cable direction ϕ_r and cable tension $f_{r,c}$. To determine this, we invert (20) to obtain the pitch angle of Bicopter i, β_i, from the ϕ_r and $f_{r,c}$. The threshold $l_{t,c}$ is then computed from β_1 and β_2 using (22) as:

$$l_{t,c} = 2d_m \sin\big((\pi - \beta_1 - \beta_2)/2\big). \quad (43)$$

Once reaching this length, the magnets are presumed engaged and position controller switches to the quadcopter mode. In this mode, the angle between the bicopters (2ζ in Figure 2(c)) is regulated by adjusting the cable length. Two bicopters are in full contact when $l_c = 0$ and $\zeta = 0$.

Transitioning back to tethered-flight mode requires breaking the strong magnetic connection, exceeding the platform's thrust capacity. To facilitate this, each bicopter is equipped with a lever structure near the magnets (see Figure 2(c)). The levers are angled such that they become in contact when the cable length is over $l_{t,c}$. This prevents them from interfering with the bicopter-to-quadcopter transition.

The transition to the tethered-flight mode begins by extending l_c. As the cable length increases and 2ζ grows, the levers get closer. The transition happens when l_c reaches $l_{t,c}$ and the levers touch at point P_l, acting as a pivot and limiting the configuration angle 2ζ from growing further. The controller is then switched to the tethered-flight mode.

Continuing to extend the cable makes the cable slack. This allows propeller thrusts to produce substantial torques about P_l. According to the previous equilibrium analysis, the torque exerted by thrust of each bicopter about P_l is proportional to the reference cable tension as $\tau_l = f_{r,c}(d_m \sin((\beta_{r,1} + \beta_{r,2})/2) + d_l)$, where d_l is the length of the levers as shown in Figure 2(c). Such torque results in a pulling force of $f_{p,m} = \tau_l/d_l = f_{r,c}((d_m/d_l)\sin((\beta_{r,1} + \beta_{r,2})/2) + 1)$ on the magnets at point P_m. When $d_m/d_l > 1$, the mechanical advantage helps the magnets disengage.

For instance, in a flight with the reference states $\beta_{r,1}, \beta_{r,2} = \pi/4$ and $f_{r,c} = 0.23(m_1 + m_2)g$, by substituting these values into the above equations with $d_m/d_l = 5$, the propeller thrusts create a pulling force of $f_{p,m} = 1.04(m_1 + m_2)g$ on the magnets. This exceeds the force required to break the magnetic connection, $0.9(m_1 + m_2)g$ (experimentally determined). Meanwhile, it is also higher than the maximum thrust of each bicopter, $0.75(m_1 + m_2)g$, which means using propelling thrust alone without mechanical advantage cannot split the two bicopters.

Once the magnetic connection is interrupted, the system then reverts to tethered-flight mode.

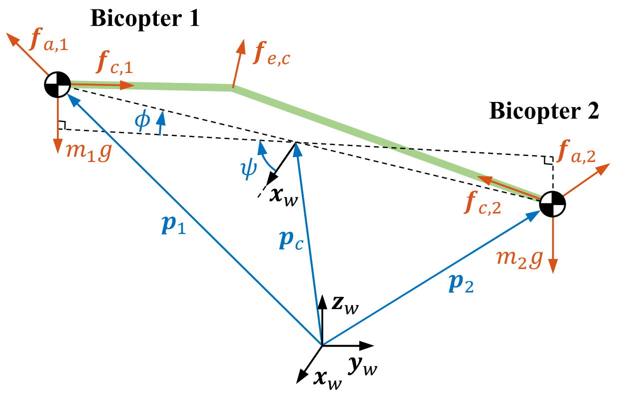

Figure 4. Schematic diagram illustrating how the platform physically interacts with objects through the cable in tethered-flight mode.

4.4 *Considerations for physical interactions*

One function of the proposed platform is its ability to physically interact with the environments using the cable in the tethered-flight mode. By modulating cable tension, the system can exert controlled forces and torques on a target.

To model the interaction, we assume that the cable is subject to an external force $\boldsymbol{f}_{e,c}$ as shown in Figure 4. This alters the cable tension felt by each bicopter, breaking the previous symmetry. We let $\boldsymbol{f}_{c,i}$ denote the cable tension of Bicopter i. The force vectors satisfy $\boldsymbol{f}_{c,1} + \boldsymbol{f}_{c,2} = \boldsymbol{f}_{e,c}$, whereas the translational dynamics, previously described by (5) becomes:

$$m_i \ddot{\boldsymbol{p}}_i = m_i \boldsymbol{g} + \boldsymbol{f}_{a,i} + \boldsymbol{f}_{c,i}. \tag{44}$$

Similar to the previous derivations, we can then obtain the equation for the CoM via (6) as:

$$(m_1 + m_2)\ddot{\boldsymbol{p}}_c = (m_1 + m_2)\boldsymbol{g} + \boldsymbol{f}_{a,1} + \boldsymbol{f}_{a,2} + \boldsymbol{f}_{e,c}. \tag{45}$$

In a similar manner, the difference between $\ddot{\boldsymbol{p}}_1$ and $\ddot{\boldsymbol{p}}_2$ describes the dynamics of the cable:

$$\frac{m_1 m_2 l_c^2}{m_1 + m_2}\ddot{\phi} = \frac{l_c(m_2 \boldsymbol{f}_{a,1} - m_1 \boldsymbol{f}_{a,2})^\top \boldsymbol{u}_\phi}{m_1 + m_2} + \tau_{e,\phi}, \tag{46}$$

$$\frac{m_1 m_2 l_c^2 \cos^2\phi}{m_1 + m_2}\ddot{\psi} = \frac{l_c(m_2 \boldsymbol{f}_{a,1} - m_1 \boldsymbol{f}_{a,2})^\top \boldsymbol{u}_\psi}{m_1 + m_2} + \tau_{e,\psi}, \tag{47}$$

where $\tau_{e,\phi}$ and $\tau_{e,\psi}$ represent the interaction torques in the respective directions:

$$\begin{aligned}\tau_{e,\phi} &= \|\boldsymbol{p}_1 - \boldsymbol{p}_c\| \boldsymbol{f}_{c,1}^\top \boldsymbol{u}_\phi - \|\boldsymbol{p}_2 - \boldsymbol{p}_c\| \boldsymbol{f}_{c,2}^\top \boldsymbol{u}_\phi \\ &= \frac{l_c(m_2 \boldsymbol{f}_{c,1} - m_1 \boldsymbol{f}_{c,2})^\top \boldsymbol{u}_\phi}{m_1 + m_2},\end{aligned} \tag{48}$$

$$\begin{aligned}\tau_{e,\psi} &= \|\boldsymbol{p}_1 - \boldsymbol{p}_c\| \boldsymbol{f}_{c,1}^\top \boldsymbol{u}_\psi - \|\boldsymbol{p}_2 - \boldsymbol{p}_c\| \boldsymbol{f}_{c,2}^\top \boldsymbol{u}_\psi \\ &= \frac{l_c(m_2 \boldsymbol{f}_{c,1} - m_1 \boldsymbol{f}_{c,2})^\top \boldsymbol{u}_\psi}{m_1 + m_2}.\end{aligned} \tag{49}$$

Finally, substituting the controller (31) into (45), (46), and (47), we yield the closed-loop dynamics:

$$\begin{aligned}\boldsymbol{f}_{e,c} &= (m_1 + m_2)(\ddot{\boldsymbol{p}}_c - \ddot{\boldsymbol{p}}_{r,c}) + \boldsymbol{K}_{p,p}(\boldsymbol{p}_c - \boldsymbol{p}_{r,c}) \\ &\quad + \boldsymbol{K}_{p,d}(\dot{\boldsymbol{p}}_c - \dot{\boldsymbol{p}}_{r,c}),\end{aligned} \tag{50}$$

$$\begin{aligned}\tau_{e,\phi} &= \frac{m_1 m_2 l_c^2}{m_1 + m_2}\ddot{\phi} + l_c^2\big(K_{\phi,p}(\phi - \phi_r) \\ &\quad + K_{\phi,d}(\dot{\phi} - \dot{\phi}_r)\big),\end{aligned} \tag{51}$$

$$\begin{aligned}\tau_{e,\psi} &= \frac{m_1 m_2 l_c^2 \cos^2\phi}{m_1 + m_2}\ddot{\psi} + l_c^2 \cos^2\phi\big(K_{\psi,p}(\psi - \psi_r) \\ &\quad + K_{\psi,d}(\dot{\psi} - \dot{\psi}_r)\big).\end{aligned} \tag{52}$$

Equations (50)–(52) reveal that, with $\boldsymbol{f}_{e,c}$ the controller in (31) functions as an impedance controller (Rashad et al. 2022), regulating the relationship between interaction forces/torques and the system. By adjusting the control gains in (50)–(52), we can achieve the desired mechanical impedance, thereby precisely controlling the interaction dynamics. This capability enables a wide range of applications, including aerial manipulation, contact-based sensing for infrastructure inspection, and controlled perching on structures as demonstrated in the experiments.

5 Flight experiments

In this section, we briefly introduce the prototype and the flight setup. Then we showcase several sets of indoor experiments to demonstrate the flight capability, mid-air transitions, and robot-environment interactions of the proposed flight system. Finally, we present outdoor flights to validate the system's robustness in real-world conditions. All demonstrations are presented in the Supplementary Video.

5.1 *Platform and experimental setup*

The constructed prototypes are presented in Figure 1. Each bicopter employs two brushless motors (GEPRC, GR1106 6000-KV) and two 3-blade propellers (Gemfan, Flash 2540) for thrust generation. Two servo motors (BlueArrow, MI CS 9-4F MG) connect the brushless motors and the 3D-printed airframe (Bambu Lab X1-Carbon, PLA Basic) to alter the thrust direction. A 4-in-1 electronic speed controller (LANNRC, 30-A) together with a flight controller (Bitcraze, Crazyflie Bolt 1.1) are integrated onto the airframe. For modularity, four cylindrical NdFeB magnets (diameter of 3 mm and thickness of 15 mm) are affixed underneath the vehicle. A LiPo battery (500-mAh 2S) is used as the power source. For Bicopter 1, a geared motor (GA12-N20 6-V 100-rpm) is equipped for driving the winch and reeling the cable, and a built-in magnetic encoder is used to measure the cable length. For Bicopter 2, a single-axis force sensor (SimBaTouch, SBT674 1-kg) is incorporated for measuring the cable tension. The two bicopters have almost the same mass of 165 g.

The experiments were performed in a flight arena equipped with ten motion capture cameras (OptiTrack, Prime 13W) to provide real-time measurements of the bicopter positions $\boldsymbol{p}_1$ and $\boldsymbol{p}_2$. In the free-flight mode, these were directly employed for position control. In the tethered-flight and quadcopter modes, we computed the CoM position of the system and the cable direction as $\boldsymbol{p}_c = (m_1\boldsymbol{p}_1 + m_2\boldsymbol{p}_2)/(m_1 + m_2)$ and $\boldsymbol{u}_c = (\boldsymbol{p}_1 - \boldsymbol{p}_2)/\|\boldsymbol{p}_1 - \boldsymbol{p}_2\|$, respectively. With this feedback, the position controller was implemented on a ground computer and executed at 100 Hz. The attitude controller was implemented on the onboard flight controller and executed at $1\,\mathrm{kHz}$, using the attitude feedback from the inertial measurement unit (IMU).

The ground computer and the flight controller communicated via radio at $100\,\mathrm{Hz}$. The computer transmitted the reference states to the flight controller for attitude control. The onboard flight controller provided the bicopter states (attitude and actuator commands) and cable states (length and tension) to the ground computer for the position controller and state detection.

5.2 Flight modes and mid-air transitions

To demonstrate the platform's capability for controlled flight in different modes and mid-air transitions, we conducted a comprehensive experiment as illustrated in Figure 5. The demo began with free-flight mode, with the bicopters taking off independently with the cable length $l_c = 1.2\,\mathrm{m}$. The reference positions $\boldsymbol{p}_{r,1}$ and $\boldsymbol{p}_{r,2}$ were set to maintain a $0.7\,\mathrm{m}$ separation in the y direction to ensure a slack cable.

At $t = 4.6\,\mathrm{s}$, the system transitioned to tethered-flight mode by switching the position controller for the system to track the reference CoM position $\boldsymbol{p}_{r,c} = [0, 0, 0.8]^\top\,\mathrm{m}$, the reference cable angles $\phi_r = 0°$ and $\psi_r = 90°$ and reference cable tension of $f_{r,c} = 0.75\,\mathrm{N}$. Immediately after switching, the two bicopters pitched away from one another, causing the pitch angle β_i to temporarily exceed $45°$ until the cable became taut. The system rapidly reached equilibrium with the desired cable tension with a pitch angle of $\beta_i \approx 40°$ within $0.7\,\mathrm{s}$.

Next, we commanded the winch to reel in the cable to reduce the separation at a rate of $8.3\,\mathrm{cm/s}$. When the cable length reduced to the transition threshold of $l_{t,c} = 0.07\,\mathrm{m}$ at $t = 20.0\,\mathrm{s}$, the magnets engaged, and the position controller was switched to the quadcopter mode. The CoM position, cable direction, and cable tension setpoints were kept unchanged. Continuing retracting the cable decreased the configuration angle 2ζ and simultaneously increased the pitch angles. When $l_c = 0\,\mathrm{m}$, the two bicopters were in full contact with a pitch angle near $90°$. The transition to the quadcopter mode took approximately $1.1\,\mathrm{s}$. Then, the quadcopter hovered in place for a few seconds ($t = 21.1 - 26.0\,\mathrm{s}$).

To reverse the transition sequence, we extended the cable at a rate of $8.3\,\mathrm{cm/s}$. When this reached the transition threshold $l_{t,c}$ at $t = 26.9\,\mathrm{s}$, the levers came in contact, and the position controller switched to the tethered-flight mode. Continued increases in the cable length then broke the magnetic connection and split the bicopters apart. This transition took $1.4\,\mathrm{s}$. The cable remained taut and continued to extend until $l_c = 1.2\,\mathrm{m}$. Finally, we commanded the platform to transition back to the free-flight mode at $t = 42.7\,\mathrm{s}$, setting the position setpoints to be $0.7\,\mathrm{m}$ apart. The swift transition to the free-flight mode took less than $0.5\,\mathrm{s}$. Shortly after, the altitude setpoint was gradually lowered for landing.

During the entire $46.0\,\mathrm{s}$ multi-mode flight, the root-mean-square (RMS) errors of the CoM position $\boldsymbol{p}_c$ in the x, y, and z directions were $2.2\,\mathrm{cm}$, $1.6\,\mathrm{cm}$, and $3.6\,\mathrm{cm}$, respectively. During the tethered-flight and quadcopter modes ($t = 4.6 - 42.7\,\mathrm{s}$), the RMS errors of the cable angles ϕ and ψ were $1.3°$ and $2.6°$, respectively. These results indicated that the platform could transition between operating modes in mid-air while maintaining bounded tracking errors (CoM position error $< 10\,\mathrm{cm}$, and cable-angle error $< 10°$ in the tensioned modes).

5.3 Flight with limited position feedback

Furthermore, an experiment was performed to demonstrate the ability of the proposed platform to work when the position feedback of only one bicopter was available. In this case, the platform cannot work in free-flight mode as in that case each bicopter needs to regulate its own position based on the position feedback. Therefore, we only carried out flights in tethered-flight and quadcopter modes.

We assumed that only position feedback of Bicopter 1 was available and set $\boldsymbol{p}_c = \boldsymbol{p}_1$ for the position control in both tethered-flight and quadcopter modes (i.e., (31) and (37)). As the terms related to the cable direction in (31) became invalid because the feedback of the cable angles relied on the relative position between the two bicopters, we omitted those cable angle feedback components in the controller, such that the cable direction was only controlled in an open-loop manner. Under the assumption that Bicopter 2 could be modeled as a planar tethered aerial robot anchored at Bicopter 1, the linearized closed-loop dynamics was locally asymptotically stable about the hovering equilibrium for sufficiently large K_p and K_d (see Supplementary Materials).

As shown in Figure 6, both bicopters started in tethered-flight mode with the cable fully extended ($l_c = 1.2\,\mathrm{m}$). The references for position, cable angle, and cable tension were set to $\boldsymbol{p}_{r,c} = \boldsymbol{p}_{r,1} = [0, 0.6, 0.8]^\top\,\mathrm{m}$, $\phi_r = 0°$, $\psi_r = 90°$, and $f_{r,c} = 0.75\,\mathrm{N}$. Without the feedback term on the cable direction, an oscillating motion of the cable was observed. Similarly, the position of Bicopter 2 was affected as the direction of the cable changed.

Next, the winch on Bicopter 1 was commanded to reel in to reduce the cable length, pulling Bicopter 2 toward Bicopter 1. The oscillation decreased as the two bicopters moved closer. At $t = 18.8\,\mathrm{s}$, the cable length reached the transition threshold $l_{t,c}$, triggering the platform to enter the quadcopter mode. The cable length continued to decrease until the two bicopters made full contact ($l_c = 0\,\mathrm{m}$).

At $t = 22.8\,\mathrm{s}$, we extended the cable to the transition threshold $l_{t,c}$ to reverse the transition. The platform successfully reverted to tethered-flight mode while the cable continued to extend until it reached $l_c = 1.2\,\mathrm{m}$. The oscillating motion of Bicopter 2 reappeared as the cable length increased.

During the entire process ($38.5\,\mathrm{s}$), Bicopter 1 tracked the reference position well, with the RMS errors in the x, y, and z directions of $1.9\,\mathrm{cm}$, $1.4\,\mathrm{cm}$, and $3.2\,\mathrm{cm}$. The RMS errors of the cable angles ϕ and ψ were $1.9°$ and $7.3°$, which were 1.5 and 2.8 times the errors when the flight was performed with full position feedback (Section 5.2) due to the nature of the open-loop control. Despite some oscillations presented at large cable lengths, these results indicated that the platform could still operate effectively without complete position feedback.

This experiment simulated real-world scenarios where imprecise position feedback, such as GPS, might be insufficient for controlling both bicopters in proximity. In such cases, position feedback for Bicopter 1 could be

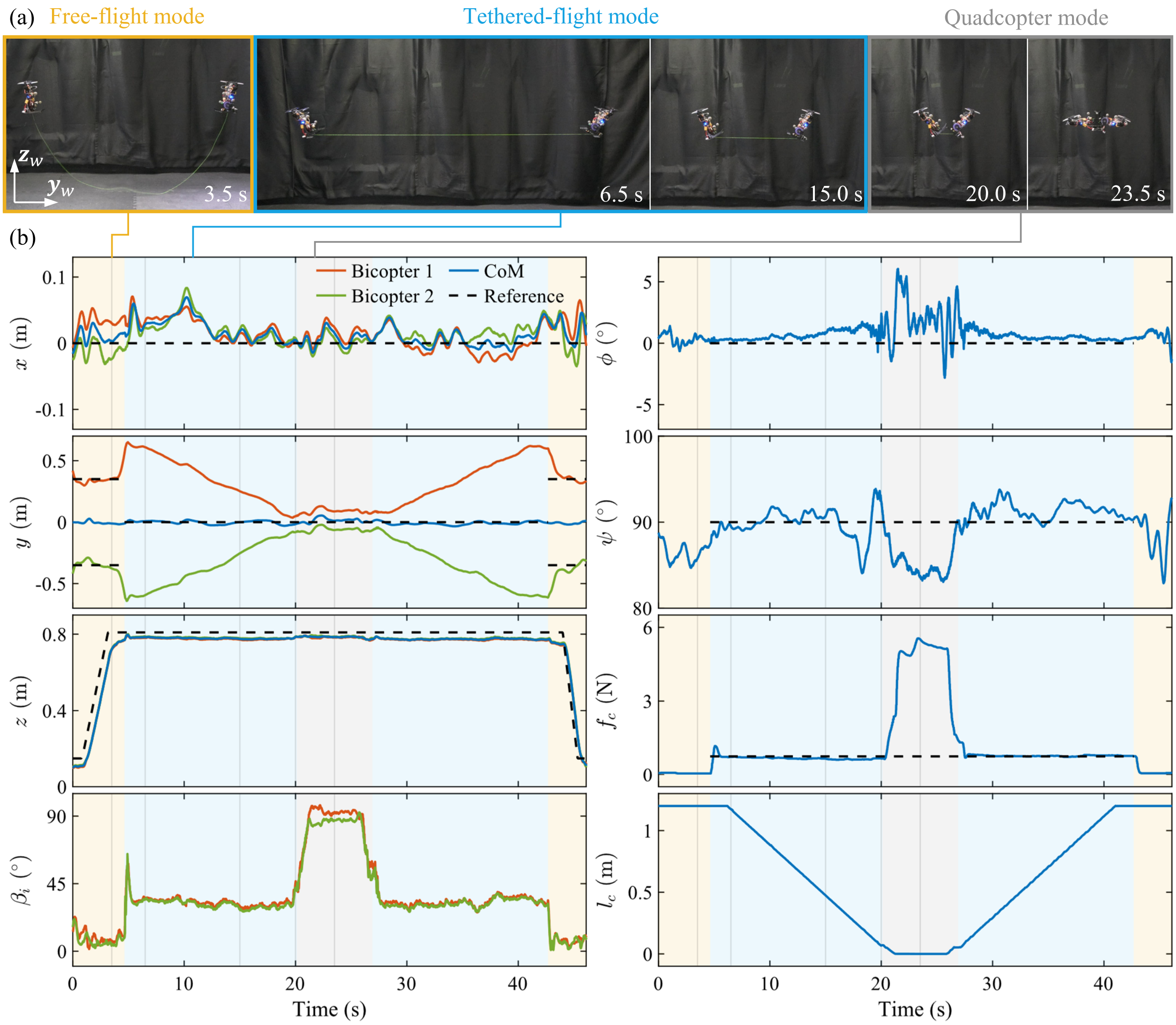

Figure 5. The platform performed a multi-mode flight with mid-air transitions. (a) Image sequence describing the flight. (b) Trajectories of the system states during the flight.

replaced with pilot commands, demonstrating the platform's robustness and adaptability in environments with limited sensing.

5.4 *Object manipulation*

To demonstrate the physical interaction capability of the proposed platform according to the analysis in Section 4.4, we showed how the platform in tethered-flight mode could be used to perform several manipulation tasks.

5.4.1 Payload transport. In the first experiment, the platform transported a suspended payload with a mass of 40 g (24% of one bicopter and 12% of the entire system) as shown in Figure 7. Initially, the bicopters flew in the tethered-flight mode with $\phi_r = 0°$, $\psi_r = 90°$, and $f_{r,c} = 0.75\,\text{N}$, approaching the payload, with a hook, from the side by varying the reference position $\boldsymbol{p}_{r,c}$ in the x direction so the cable was below the handle. Next, from $t = 2.8\,\text{s}$, the system followed a reference trajectory of $\boldsymbol{p}_{r,c}$ to pull up the payload and translated toward the desired location. As seen in Figure 7(b), the thrusts of both bicopters increased notably when the system carried the payload. Upon reaching the desired location, the altitude setpoint was lowered to drop off the payload at $t = 19.8\,\text{s}$.

For the period the system was not lifting the payload ($t = 0.0 - 2.8\,\text{s}$ and $t = 19.8 - 22.0\,\text{s}$), the RMS errors of the CoM position in the x, y, and z directions were 4.2 cm, 1.9 cm, and 2.6 cm, respectively. With the payload ($t = 2.8 - 19.8\,\text{s}$), these changed to 2.7 cm, 6.3 cm, and 7.2 cm, respectively. The amplified errors in the y and z directions were anticipated and could be explained by the impedance control strategy in (50). Despite the increased error, the system remained stable and robust throughout the demonstration.

To demonstrate scalability and increased payload capability, we replaced the original brushless motors with higher-KV units (GEPRC, GR1106 7500-KV) and repeated the payload lifting experiment with a heavier load. As shown in Figure 8, the platform lifted a 100 g payload ($\approx 30\%$ of the total system mass) while maintaining stable flight without modification to the platform structure or control framework.

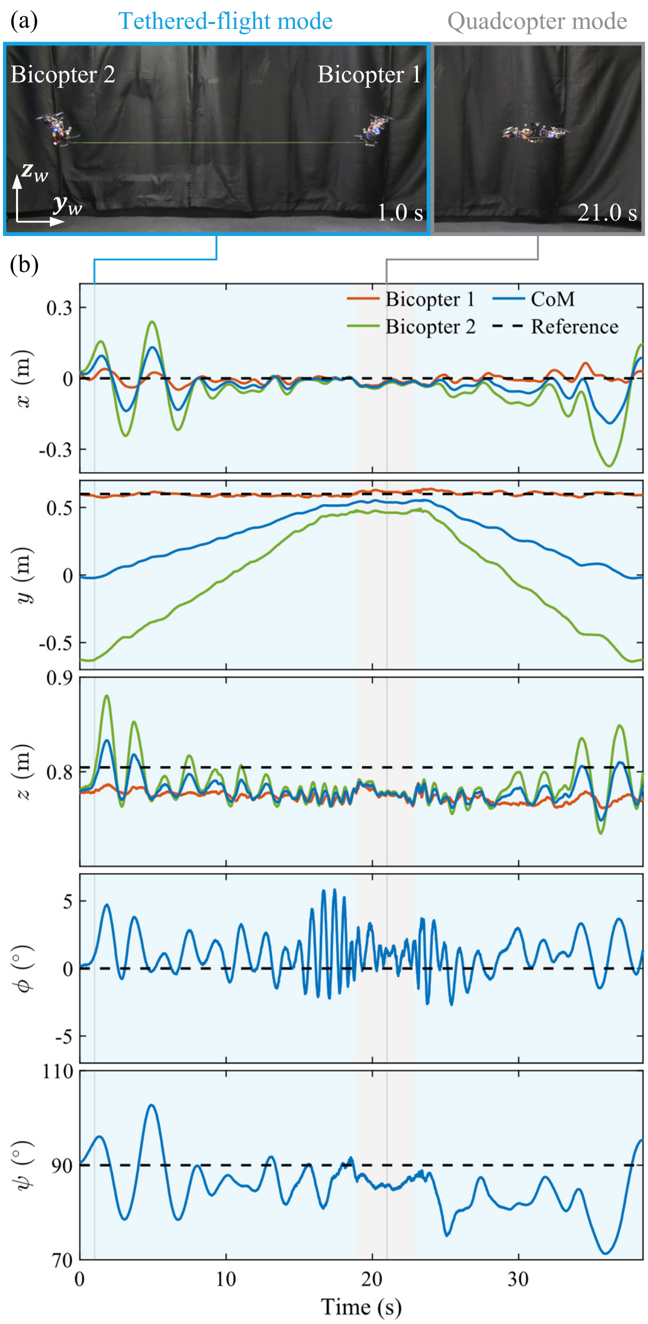

Figure 6. The platform performed a multi-mode flight with mid-air transitions using only position feedback of Bicopter 1. (a) Image sequence describing the flight. (b) Trajectories of the system states during the flight.

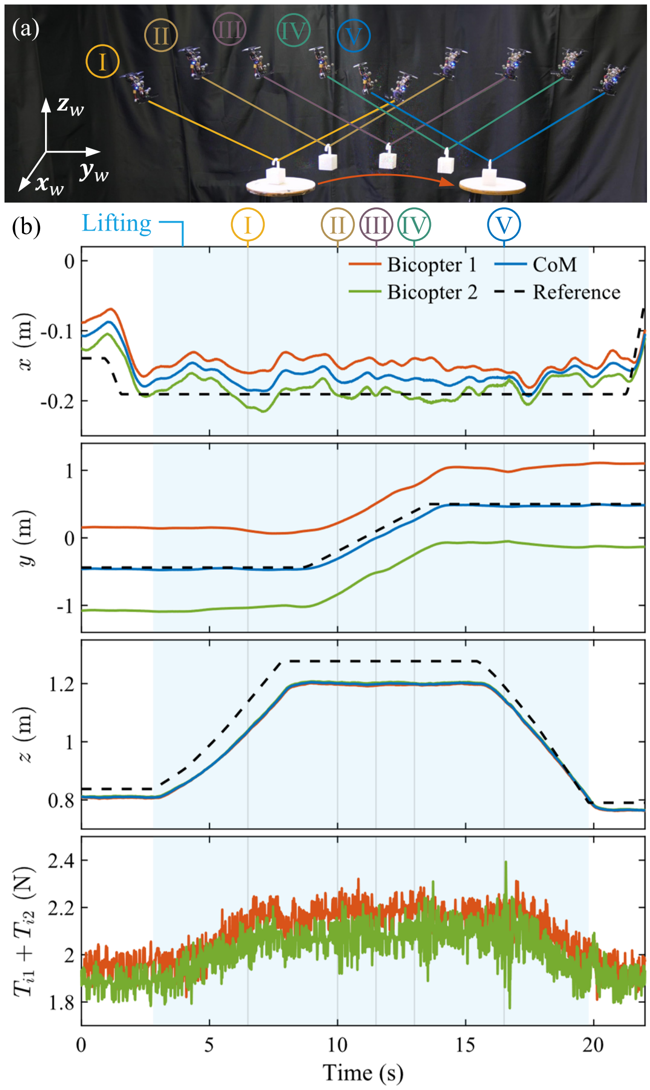

Figure 7. The platform utilized the cable to transport a suspended payload. (a) Composite image describing the platform's motion. (b) Trajectories of the system states during the experiment.

However, increasing thrust capability likely reduced flight endurance (Bauersfeld and Scaramuzza 2022).

5.4.2 Valve rotation. In this experiment, the platform exploited the cable to turn a rotary hand pump, as captured in Figure 9. The bicopters first hovered above the pump in tethered-flight mode with $\phi_r = 0°$, $\psi_r = 90°$, and $f_{r,c} = 0.75\,\mathrm{N}$. The altitude setpoint was decreased for the system to approach the pump handle. Upon reaching the handle position at $t = 2.9\,\mathrm{s}$, the entire platform rotated around the vertical axis at a fixed reference CoM position $\boldsymbol{p}_{r,c} = [-0.55, 0, 0.91]^\top\,\mathrm{m}$ while the reference cable angle ψ_r varied. The cable contacted the handle, resulting a torque and rotation. After rotating the handle by over one and a half cycles at $t = 21.9\,\mathrm{s}$, the angle setpoint switched the direction. Then the cable disengaged from the handle and the pump.

The RMS error of the cable angle ψ was $8.5°$ in the period the system was not in contact with the pump ($t = 0.0 - 2.9\,\mathrm{s}$ and $t = 21.9 - 24.7\,\mathrm{s}$). This elevated to $20.1°$ when the torque was exerted ($t = 2.9 - 21.9\,\mathrm{s}$). The results of these two experiments demonstrated that the proposed platform could successfully perform manipulation tasks utilizing the tethered-flight mode.

5.5 Branch perching

The platform was also able to perch on horizontal rails using the cable. Two experiments were conducted to demonstrate this capability: guided cable-wrapping perching and dynamic perching.

5.5.1 Guided perching through cable wrapping. In the first experiment, the system sequentially wrapped the cable around a branch for perching as presented in Figure 10. Initially, the bicopters approached the branch from below in tethered-flight mode, with the reference cable direction

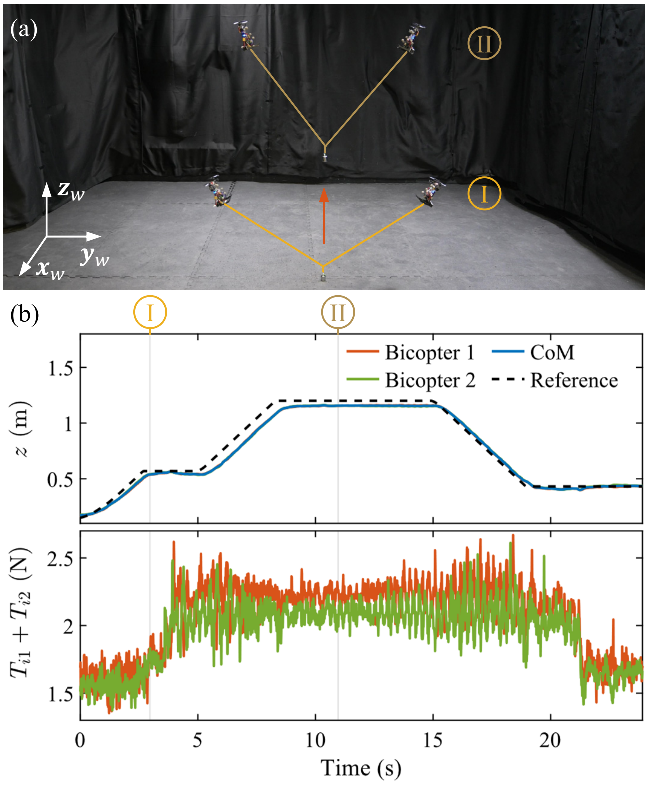

Figure 8. Payload lifting experiment with a $100\,\mathrm{g}$ load using the cable. (a) Composite image of the maneuver. (b) Trajectories of the system states during the experiment.

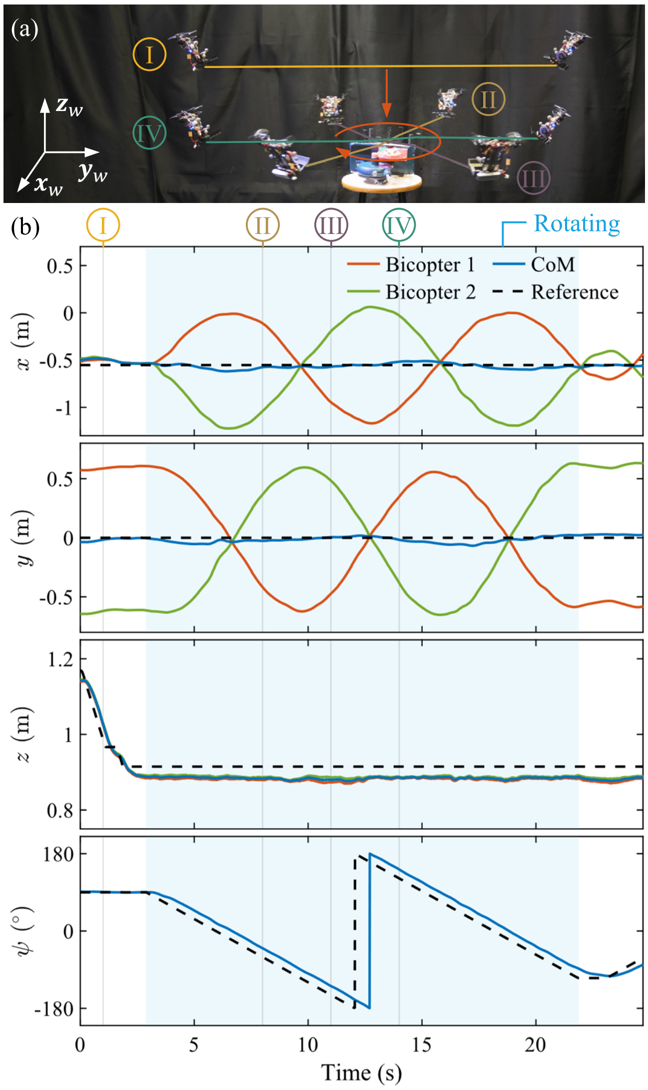

Figure 9. The platform exploited the cable to turn a rotary hand pump. (a) Composite image describing the platform's motion. (b) Trajectories of the system states during the experiment.

perpendicular to the branch ($\phi_r = 0°$ and $\psi_r = 90°$) and $f_{r,c} = 0.75\,\mathrm{N}$. Next, the altitude setpoint (z component of $\boldsymbol{p}_{r,c}$) was raised until the two bicopters were above the branch. This was followed by a change in the cable reference angle ψ_r to command the bicopters to circle around the vertical axis and wrap the cable. After slightly lowering the altitude setpoint, the position controller of the system was disabled at $t = 20.8\,\mathrm{s}$, leaving only the attitude controller to stabilize the bicopters. Then, the reference pitch angles $\beta_{r,i}$ of both bicopters were gradually increased, and the axial thrust reference $T^{(z)}_{r,i}$ was set to a constant value of $1.3\,\mathrm{N}$. According to the equilibrium relation (18), this allowed the bicopters to steadily fall (ϕ increasing for Bicopter 1 and decreasing for Bicopter 2). When the cable became almost vertical and the two bicopters were suspended upside down, the system was powered off at $t = 31.9\,\mathrm{s}$, entering the power-conserving state.

To take off and resume operation, the bicopter was instructed to repeat the above sequence in reverse order. At $t = 37.7\,\mathrm{s}$, the propulsion was turned on, and the attitude controller was reactivated. After the cable reached the horizontal configuration by gradually decreasing $\beta_{r,i}$ at $t = 44.9\,\mathrm{s}$, the position controller was enabled, and the bicopters returned to the tether-flight mode. Finally, the system circled around the vertical axis to unwind the cable from the branch and then lowered its altitude to leave the branch.

5.5.2 Dynamic perching. In this experiment, we showed that the bicopters could utilize the swing dynamics to wrap the cable around a branch for perching with minimal active control as depicted in Figure 11. Initially, the system hovered $1.8\,\mathrm{m}$ away from the rail in tethered-flight mode with the reference CoM altitude level with the rail and the cable direction parallel with the branch ($\phi_r = 0°$ and $\psi_r = 180°$) and $f_{r,c} = 0.75\,\mathrm{N}$. To prepare for the approach, the reference elevation cable angle ϕ_r was altered from $0°$ to $-35°$, positioning the bicopters above and below the rail as seen in Figure 11(a). Next, the system sped toward the rail following the changing reference position $\boldsymbol{p}_{r,c}$ with a maximum speed of $3.0\,\mathrm{m/s}$. The contact with the rail at $t = 6.2\,\mathrm{s}$ was detected through the measured cable tension, with a prespecified threshold of $2.0\,\mathrm{N}$. The detection triggered the bicopters to switch off all propellers and enter the resting state. Due to the residual kinetic energy, the two bicopters dynamically swung around the rail, wrapping the cable around and completing the perching motion with minimal control effort.

To take off, the attitude controller was first activated at $t = 21.4\,\mathrm{s}$, with a constant axial thrust reference $T^{(z)}_{r,i} = 1.3\,\mathrm{N}$. Then the reference pitch angles $\beta_{r,i}$ were gradually decreased to elevate the altitude of the two bicopters. At $t = 28.0\,\mathrm{s}$, the position controller of the system was activated,

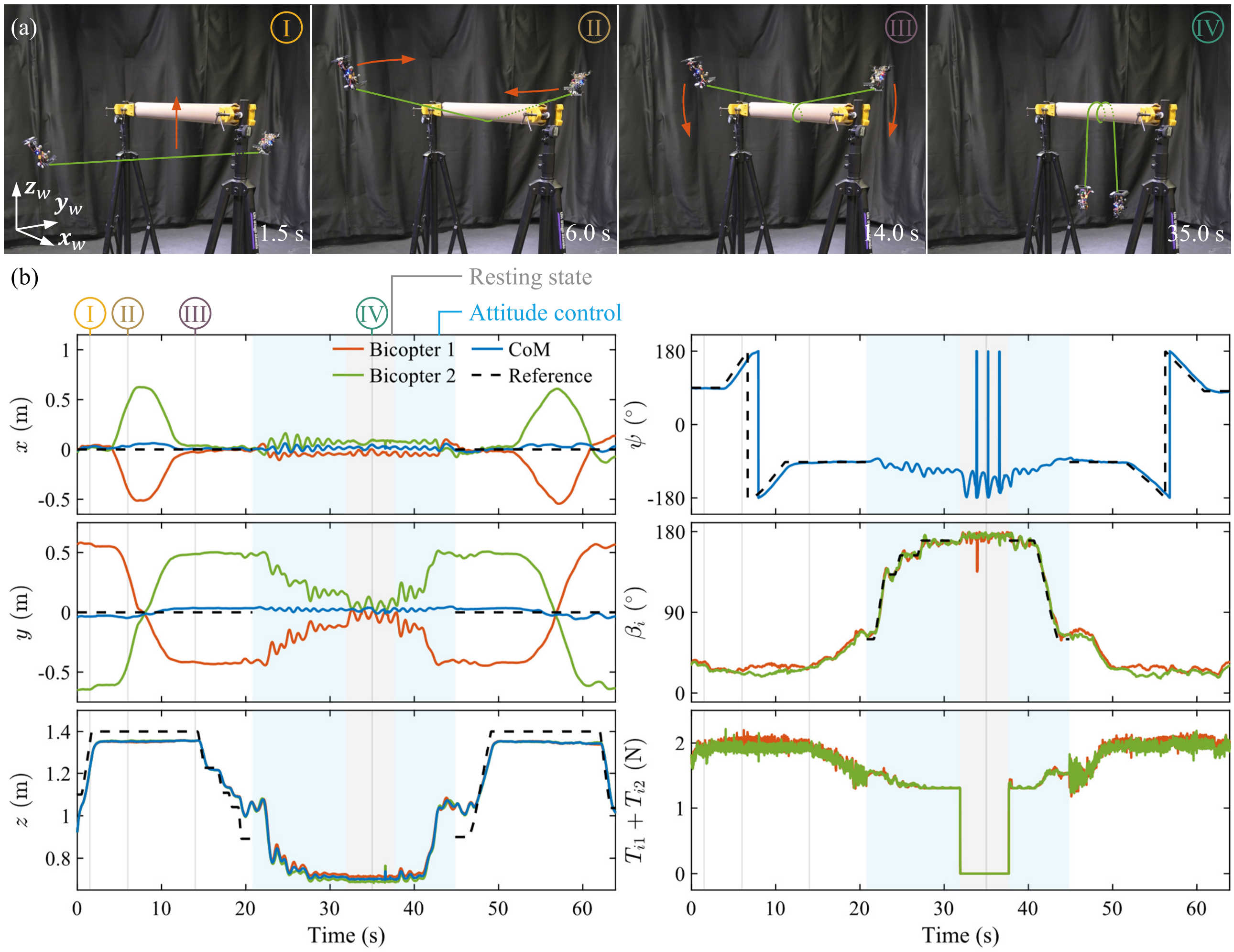

Figure 10. The platform performed guided perching through cable wrapping. (a) Image sequence describing the perching process. (b) Trajectories of the system states during the perching process.

and the bicopters entered tethered-flight mode before getting away from the rail.

These experiments demonstrated the platform's versatile perching capabilities without requiring additional grippers or actuators. The guided perching experiment showcased precise, multi-step control to wrap the cable, while the dynamic perching leveraged swing dynamics for efficient, minimal-control perching. In particular, the dynamic perching in this work enabled high-speed perching without actively controlling the perching motion, which was unique from existing implementations that required dedicated grippers to delicately absorb impact energy and simultaneously engage with the perching target in a short time (Roderick et al. 2021; Zufferey et al. 2022; Chen et al. 2022). These demonstrations highlighted the platform's adaptability and potential for lightweight, robust aerial applications.

5.6 Narrow gap passing

This experiment demonstrated how the transformable design enabled traversal of confined spaces by selecting a mode with a favorable effective cross section.

Each bicopter had dimensions of 8.0 cm (length), 17.0 cm (width), and 13.5 cm (height). Different flight modes led to different cross-sectional dimensions. In free-flight mode, each bicopter had an 8.0 cm × 13.5 cm (width×height) profile in equilibrium. In quadcopter mode, the two bicopters were docked, resulting in a 17.0 cm × 8.0 cm profile for the combined platform. These complementary profiles allowed the platform to pass through gaps with different aspect ratios.

5.6.1 Free-flight mode. In the first experiment, Bicopter 1 was commanded to track $\boldsymbol{p}_{r,1}$ and pass through a 12.0 cm × 21.0 cm (width×height) gap and return, while Bicopter 2 hovered, as shown in Figure 12(a). Over the 13.0 s maneuver, the RMS position errors of Bicopter 1 along the gap width and height were 1.7 cm and 0.5 cm, respectively. This showed that the two bicopters could move and be controlled independently, allowing one vehicle to pass through a confined opening while the other maintained a hover elsewhere.

5.6.2 Quadcopter mode. In the second experiment, the docked platform (quadcopter mode) was commanded to track the CoM reference $\boldsymbol{p}_{r,c}$ and pass through a 21.0 cm × 12.0 cm gap, as shown in Figure 12(b). During the maneuver, minor contact between the propeller and the gap boundary was observed. However, this did not result in flight instability, suggesting robustness to minor disturbances. Over the 7.0 s maneuver, the RMS CoM position errors

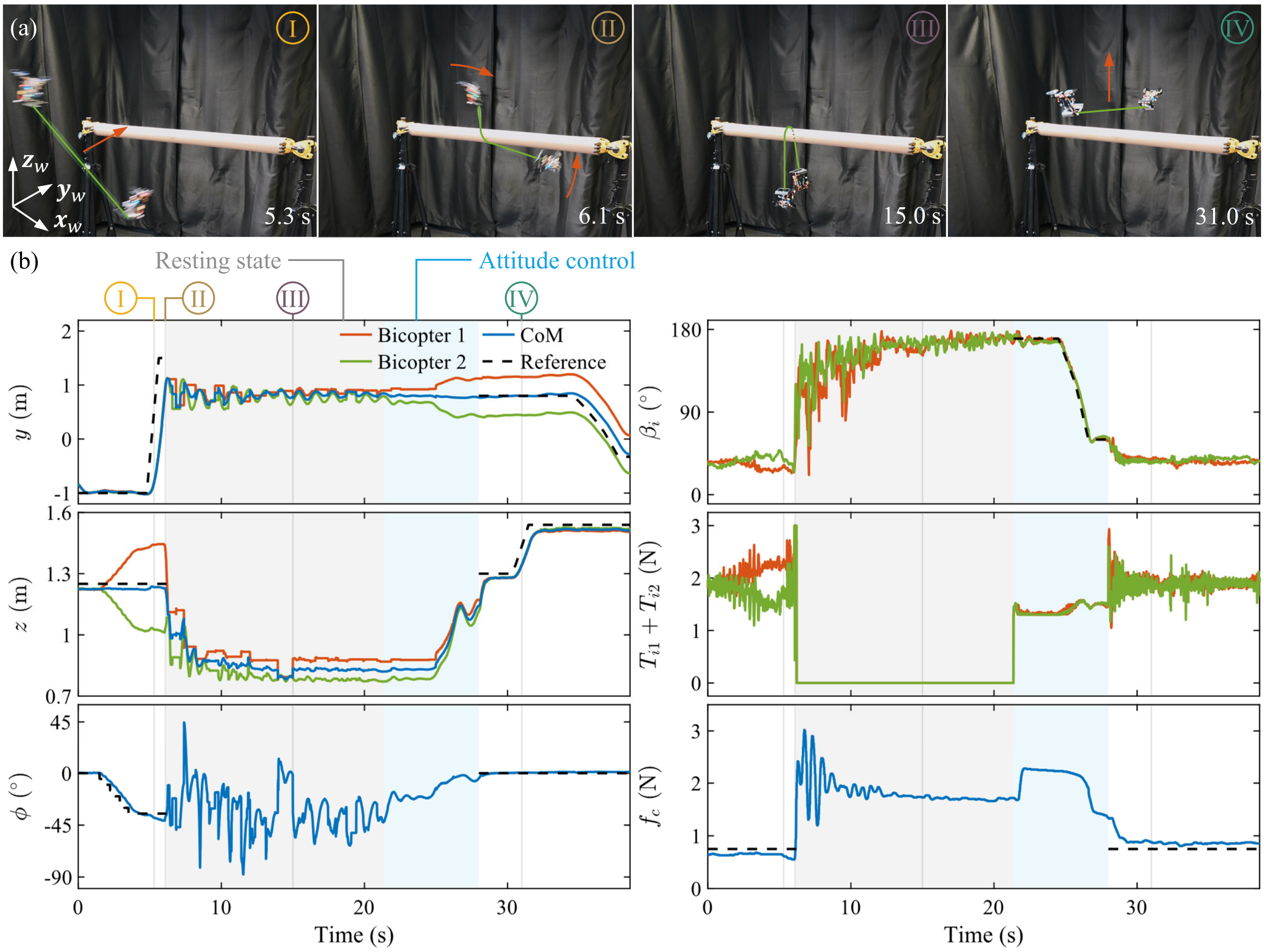

Figure 11. The platform performed dynamic perching utilizing swing dynamics. (a) Image sequence describing the perching process. (b) Trajectories of the system states during the perching process.

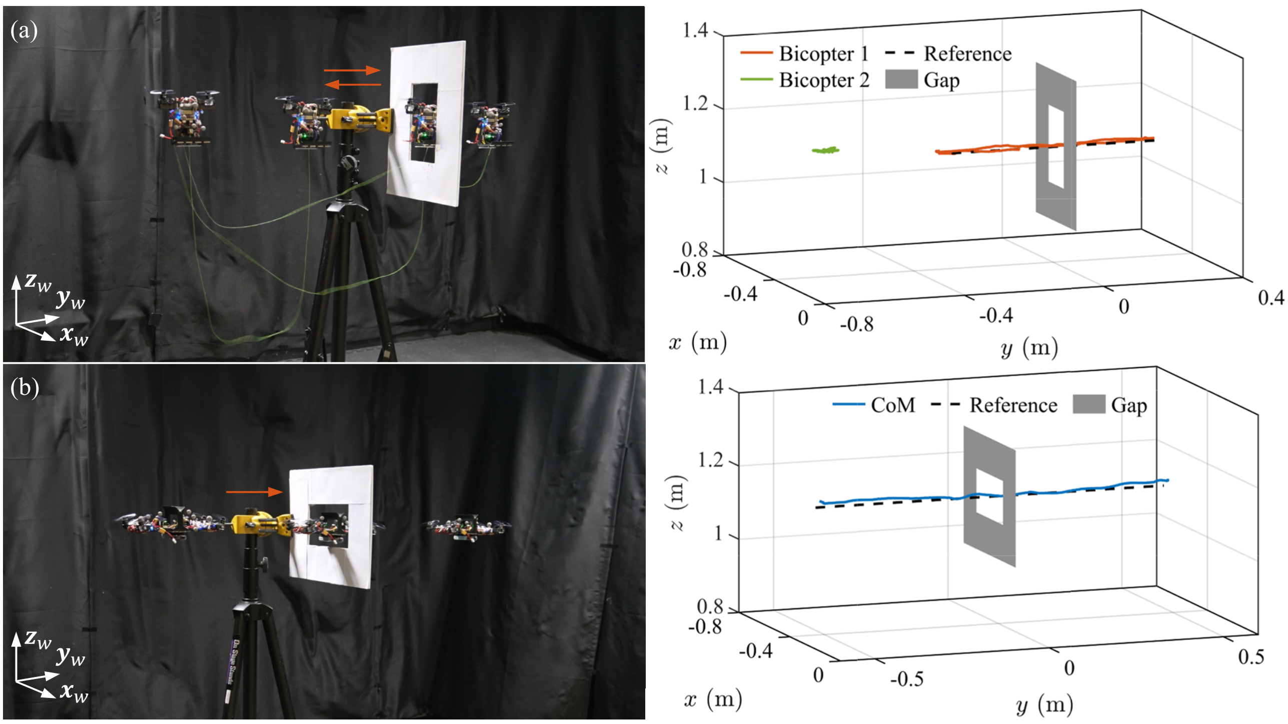

Figure 12. Composite images (left) and flight trajectories (right) of the narrow gap passing experiments. (a) Free-flight mode, where Bicopter 1 passes through a narrow, tall $(12.0\,\mathrm{cm} \times 21.0\,\mathrm{cm})$ gap and returns while Bicopter 2 hovers. (b) Quadcopter mode, where the docked platform passes through a wide, short $(21.0\,\mathrm{cm} \times 12.0\,\mathrm{cm})$ gap.

along the gap width and height were $2.1\,\mathrm{cm}$ and $1.1\,\mathrm{cm}$, respectively.

5.7 Outdoor flights

To further demonstrate the robustness of the proposed platform towards real-world applications, we conducted several flights in an outdoor environment. Each bicopter was equipped with a real-time kinematic (RTK) positioning module (Beitian, BT-468) for positioning.

5.7.1 Mid-air transitions. In the first experiment, the platform performed a multi-mode flight with mid-air transitions, as shown in Figure 13(a). Initially, the platform took off in free-flight mode and ascended to an altitude of $0.7\,\mathrm{m}$. The platform maintained its CoM position ($\boldsymbol{p}_{r,c} = [0, 0, 0.7]^\top\,\mathrm{m}$, $\phi_r = 0°$, $\psi_r = 180°$, and $f_{r,c} = 0.89\,\mathrm{N}$) while performing a sequence of mode transitions, from free-flight mode to tethered-flight mode and then to quadcopter mode over $26.0\,\mathrm{s}$. Finally, we repeated the above transition sequence in reverse order before descending for landing. Throughout the flight, the RMS errors of the CoM position in the x, y, and z directions were $7.3\,\mathrm{cm}$, $4.9\,\mathrm{cm}$, and $5.6\,\mathrm{cm}$, respectively.

5.7.2 Payload transport. In the second experiment, the platform performed a payload transport task, as shown in Figure 13(b). Initially, the platform flew in free-flight mode, approaching the payload (identical to the one used in Section 5.4.1) from the side (y direction). When the cable was below the handle, the platform transitioned to tethered-flight mode ($\phi_r = 0°$, $\psi_r = 180°$, and $f_{r,c} = 0.89\,\mathrm{N}$) and lifted the payload while following the reference CoM trajectory $\boldsymbol{p}_{r,c}$. After transporting the payload for $2.4\,\mathrm{m}$, the platform released it, transitioned back to free-flight mode, and departed from the side. During the entire $37.5\,\mathrm{s}$ transport operation, the RMS errors of the CoM position in the x, y, and z directions were $9.6\,\mathrm{cm}$, $6.2\,\mathrm{cm}$, and $9.8\,\mathrm{cm}$, respectively.

These outdoor experiments showed increased position tracking errors relative to indoor flights, which we attributed to the limited accuracy of RTK-GPS positioning and external disturbances (e.g., wind gusts).

6 Discussion and Conclusion

In this work, we presented a transformable tethered aerial platform capable of multi-mode flight. The proposed design leveraged the cable to transition between different operating modes, eliminating the need for additional reconfiguration mechanisms. Utilizing the cable as the end effector, the proposed design also allowed the system to physically interact with the environments, eliminating the need for additional grippers or actuators. To fully exploit the capabilities of the proposed system, we derived the dynamic model of the platform and developed the control methods for each mode. The developed controller ensured stable flight in each mode and also enabled the platform to operate with limited position feedback. The experimental results validated the feasibility of the proposed transformable design and highlighted the physical interaction capability of the platform.

Conventional multi-robot tethered systems are well suited to tasks that benefit from a spatially distributed configuration, including cooperative payload transport (Gassner et al. 2017; D'antonio et al. 2021; Dong et al. 2023) and multi-cable object manipulation (Sanalitro et al. 2020; Li et al. 2025; Sun et al. 2025). The proposed platform is not intended to replace these systems or to provide greater manipulation authority. Instead, its unique capability lies in task-dependent reconfiguration of the same aerial platform. The separated configurations enable the two bicopters to retain independent mobility and perform tether-based interaction, whereas the docked configuration provides a compact geometric profile for traversing confined spaces. This allows the platform to change both its geometric footprint and mechanical topology during an access-then-interact mission, instead of maintaining a distributed multi-vehicle configuration throughout operation. The gap passing experiments illustrate this advantage: the free-flight and quadcopter modes provide different effective cross-sectional profiles, enabling traversal of openings with different aspect ratios. Combined with the cable-based manipulation and perching capabilities demonstrated in this work, such reconfigurability is particularly relevant to inspection and interaction tasks in cluttered or confined environments, where both access and subsequent physical interaction may be required.

Despite these promising results, the current system has several limitations. The transformable architecture is limited to two bicopters and three predefined configurations, whereas conventional multi-robot tethered systems can accommodate more general distributed arrangements (Dong et al. 2023; Li et al. 2025; Sun et al. 2025). The flight controller is derived under static equilibrium assumptions, restricting its performance to non-aggressive maneuvers. Additionally, using the cable as an end effector imposes constraints on the shape and structure of target objects and environments. Moreover, force regulation and contact estimation are not addressed here because cable deformation during contact would require additional cable sensing and estimation modules. The platform also relies on human pilot assistance for interaction tasks, lacking autonomous perception and motion planning.

Future work will address these limitations by incorporating perception, motion planning, and cable sensing/estimation to enable more autonomous and quantitatively validated interaction control. In parallel, we will investigate aerial docking and undocking mechanisms that allow multiple aerial modules to connect through cables and form more general topological structures.

Declaration of conflicting interests

The author(s) declared no potential conflicts of interest with respect to the research, authorship, and/or publication of this article.

Funding

The author(s) disclosed receipt of the following financial support for the research, authorship, and/or publication of this article: This work was supported by the Research Grants Council of the Hong Kong Special Administrative Region of China (grant no. CityU 11218022, CityU 11217923, and PolyU R5006-23).

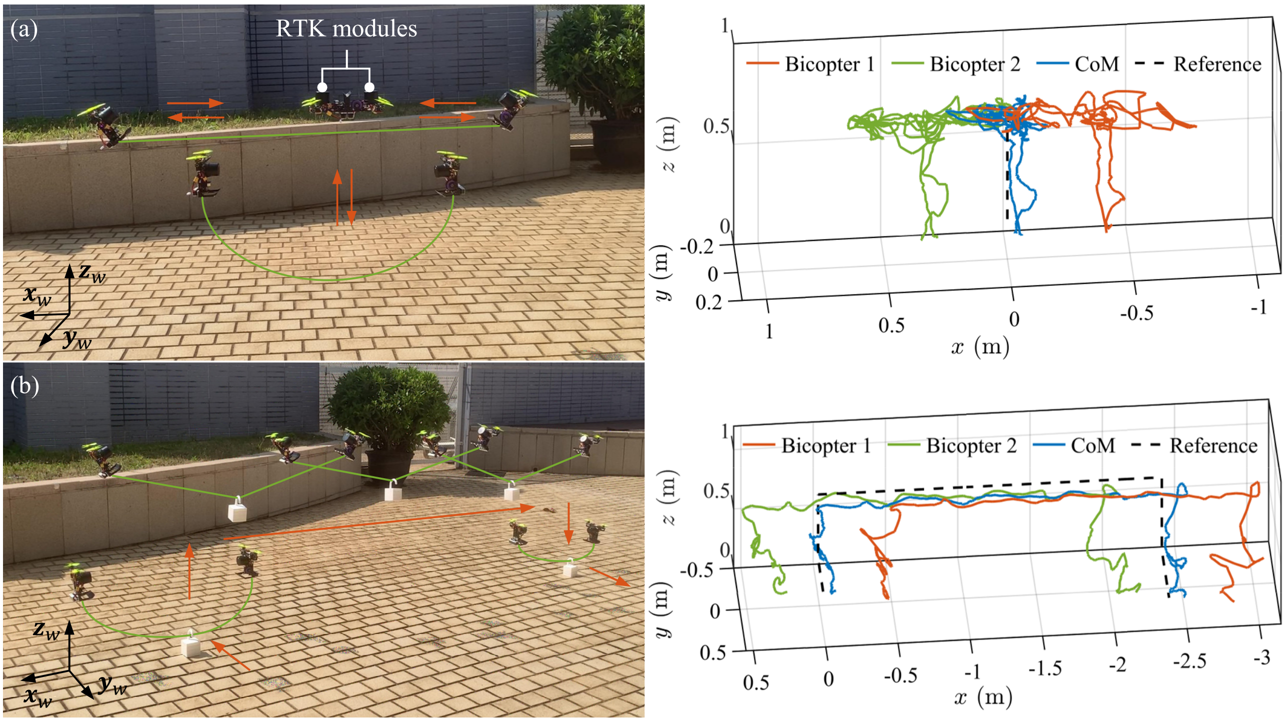

Figure 13. Composite images (left) and flight trajectories (right) of the outdoor experiments. (a) The platform performed a multi-mode flight with mid-air transitions. (b) The platform utilized the cable to transport a suspended payload.

References

Allenspach M, Bodie K, Brunner M, Rinsoz L, Taylor Z, Kamel M, Siegwart R and Nieto J (2020) Design and optimal control of a tiltrotor micro-aerial vehicle for efficient omnidirectional flight. *The International Journal of Robotics Research* 39(10-11): 1305–1325.

Aucone E, Kirchgeorg S, Valentini A, Pellissier L, Deiner K and Mintchev S (2023) Drone-assisted collection of environmental DNA from tree branches for biodiversity monitoring. *Science Robotics* 8(74): eadd5762.

Augugliaro F, Mirjan A, Gramazio F, Kohler M and D'Andrea R (2013) Building tensile structures with flying machines. In: *IEEE/RSJ International Conference on Intelligent Robots and Systems (IROS)*. pp. 3487–3492.

Bai S and Chirarattananon P (2022) SplitFlyer air: A modular quadcopter that disassembles into two bicopters mid-air. *IEEE/ASME Transactions on Mechatronics* 27(6): 4729–4740.

Bauersfeld L and Scaramuzza D (2022) Range, endurance, and optimal speed estimates for multicopters. *IEEE Robotics and Automation Letters* 7(2): 2953–2960.

Bodie K, Brunner M, Pantic M, Walser S, Pfändler P, Angst U, Siegwart R and Nieto J (2020) Active interaction force control for contact-based inspection with a fully actuated aerial vehicle. *IEEE Transactions on Robotics* 37(3): 709–722.

Brescianini D and D'Andrea R (2018) Computationally efficient trajectory generation for fully actuated multirotor vehicles. *IEEE Transactions on Robotics* 34(3): 555–571.

Bucki N, Tang J and Mueller MW (2023) Design and control of a midair-reconfigurable quadcopter using unactuated hinges. *IEEE Transactions on Robotics* 39(1): 539–557.

Cardona GA, D'Antonio DS, Vasile CI and Saldaña D (2021) Non-prehensile manipulation of cuboid objects using a catenary robot. In: *IEEE/RSJ International Conference on Intelligent Robots and Systems (IROS)*. pp. 5270–5275.

Chen TG, Hoffmann KA, Low JE, Nagami K, Lentink D and Cutkosky MR (2022) Aerial grasping and the velocity sufficiency region. *IEEE Robotics and Automation Letters* 7(4): 10009–10016.

Cheng HH and Lau D (2023) Cable attachment optimization for reconfigurable cable-driven parallel robots based on various workspace conditions. *IEEE Transactions on Robotics* 39(5): 3759–3775.

Choi SY, Choi BH, Jeong SY, Gu BW, Yoo SJ and Rim CT (2014) Tethered aerial robots using contactless power systems for extended mission time and range. In: *IEEE Energy Conversion Congress and Exposition (ECCE)*. pp. 912–916.

Cuniato E, Geckeler C, Brunner M, Strübin D, Bähler E, Ospelt F, Tognon M, Mintchev S and Siegwart R (2023) Design and control of a micro overactuated aerial robot with an origami delta manipulator. In: *IEEE International Conference on Robotics and Automation (ICRA)*. pp. 5352–5358.

Dong K, Ding R, Bai S, Cai X and Chirarattananon P (2023) Stabilizing aerodynamic dampers for cooperative transport of a suspended payload with aerial robots. *Advanced Intelligent Systems* 5(9): 2300112.

D'Antonio DS, Bhattacharya S and Saldaña D (2023) Forming and controlling hitches in midair using aerial robots. In: *IEEE International Conference on Robotics and Automation (ICRA)*. pp. 1270–1276.

D'antonio DS, Cardona GA and Saldaña D (2021) The catenary robot: Design and control of a cable propelled by two quadrotors. *IEEE Robotics and Automation Letters* 6(2): 3857–3863.

Estrada MA, Mintchev S, Christensen DL, Cutkosky MR and Floreano D (2018) Forceful manipulation with micro air vehicles. *Science Robotics* 3(23): eaau6903.

Falanga D, Kleber K, Mintchev S, Floreano D and Scaramuzza D (2018) The foldable drone: A morphing quadrotor that can squeeze and fly. *IEEE Robotics and Automation Letters* 4(2): 209–216.

Floreano D and Wood RJ (2015) Science, technology and the future of small autonomous drones. *Nature* 521(7553): 460–466.

Gassner M, Cieslewski T and Scaramuzza D (2017) Dynamic collaboration without communication: Vision-based cable-suspended load transport with two quadrotors. In: *IEEE International Conference on Robotics and Automation (ICRA)*. pp. 5196–5202.

Gu BW, Choi SY, Choi YS, Cai G, Seneviratne L and Rim CT (2016) Novel roaming and stationary tethered aerial robots for continuous mobile missions in nuclear power plants. *Nuclear Engineering and Technology* 48(4): 982–996.

Jia H, Bai S and Chirarattananon P (2023a) Aerial manipulation via modular quadrotors with passively foldable airframes. *IEEE/ASME Transactions on Mechatronics* 28(4): 1930–1938.

Jia H, Ding R, Dong K, Bai S and Chirarattananon P (2023b) Quadrolltor: A reconfigurable quadrotor with controlled rolling and turning. *IEEE Robotics and Automation Letters* 8(7): 4052–4059.

Lee AJ, Song W, Yu B, Choi D, Tirtawardhana C and Myung H (2023) Survey of robotics technologies for civil infrastructure inspection. *Journal of Infrastructure Intelligence and Resilience* 2(1): 100018.

Lee D, Kim B and Kim HJ (2025) Autonomous aerial manipulation at arbitrary pose in SE(3) with robust control and whole-body planning. *The International Journal of Robotics Research* DOI: 10.1177/02783649251378195.

Li G, Liu X and Loianno G (2025) Human-aware physical human-robot collaborative transportation and manipulation with multiple aerial robots. *IEEE Transactions on Robotics* 41: 762–781.

Li S, Liu F, Gao Y, Xiang J, Tu Z and Li D (2023) AirTwins: Modular bi-copters capable of splitting from their combined quadcopter in midair. *IEEE Robotics and Automation Letters* 8(9): 6068–6075.

Liu X, Dou M, Yan R, Huang D, Gao S, Wang B, Cui J, Ren Q, Dou L, Gao Z, Chen J and Chen BM (2024) TJ-FlyingFish: An unmanned morphable aerial-aquatic vehicle system. *Unmanned Systems* 12(02): 409–428.

Lupashin S and D'Andrea R (2013) Stabilization of a flying vehicle on a taut tether using inertial sensing. In: *IEEE/RSJ International Conference on Intelligent Robots and Systems*. pp. 2432–2438.

Mellinger D, Michael N and Kumar V (2012) Trajectory generation and control for precise aggressive maneuvers with quadrotors. *The International Journal of Robotics Research* 31(5): 664–674.

Michieletto G, Ryll M and Franchi A (2018) Fundamental actuation properties of multirotors: Force-moment decoupling and fail-safe robustness. *IEEE Transactions on Robotics* 34(3): 702–715.

Nguyen H and Alexis K (2021) Forceful aerial manipulation based on an aerial robotic chain: Hybrid modeling and control. *IEEE Robotics and Automation Letters* 6(2): 3711–3719.

Park S, Lee J, Ahn J, Kim M, Her J, Yang GH and Lee D (2018) ODAR: Aerial manipulation platform enabling omnidirectional wrench generation. *IEEE/ASME Transactions on mechatronics* 23(4): 1907–1918.

Pretto A, Aravecchia S, Burgard W, Chebrolu N, Dornhege C, Falck T, Fleckenstein F, Fontenla A, Imperoli M, Khanna R, Liebisch F, Lottes P, Milioto A, Nardi D, Nardi S, Pfeifer J, Popović M, Potena C, Pradalier C, Rothacker-Feder E, Sa I, Schaefer A, Siegwart R, Stachniss C, Walter A, Winterhalter W, Wu X and Nieto J (2020) Building an aerial-ground robotics system for precision farming: An adaptable solution. *IEEE Robotics & Automation Magazine* 28(3): 29–49.

Qin Y, Xu W, Lee A and Zhang F (2020) Gemini: A compact yet efficient bi-copter UAV for indoor applications. *IEEE Robotics and Automation Letters* 5(2): 3213–3220.

Rashad R, Bicego D, Zult J, Sanchez-Escalonilla S, Jiao R, Franchi A and Stramigioli S (2022) Energy aware impedance control of a flying end-effector in the port-Hamiltonian framework. *IEEE Transactions on Robotics* 38(6): 3936–3955.

Riviere V, Manecy A and Viollet S (2018) Agile robotic fliers: A morphing-based approach. *Soft Robotics* 5(5): 541–553.

Roderick WR, Cutkosky MR and Lentink D (2021) Bird-inspired dynamic grasping and perching in arboreal environments. *Science Robotics* 6(61): eabj7562.

Ryll M, Muscio G, Pierri F, Cataldi E, Antonelli G, Caccavale F, Bicego D and Franchi A (2019) 6D interaction control with aerial robots: The flying end-effector paradigm. *The International Journal of Robotics Research* 38(9): 1045–1062.

Sanalitro D, Savino HJ, Tognon M, Cortés J and Franchi A (2020) Full-pose manipulation control of a cable-suspended load with multiple UAVs under uncertainties. *IEEE Robotics and Automation Letters* 5(2): 2185–2191.

Schedl DC, Kurmi I and Bimber O (2021) An autonomous drone for search and rescue in forests using airborne optical sectioning. *Science Robotics* 6(55): eabg1188.

Sun S, Wang X, Sanalitro D, Franchi A, Tognon M and Alonso-Mora J (2025) Agile and cooperative aerial manipulation of a cable-suspended load. *Science Robotics* 10(107): eadu8015.

Tang J and Mueller MW (2025) PairTilt: Design and control of an active tilt-rotor quadcopter for improved efficiency and agility. *Advanced Intelligent Systems* : 2400494.

Tognon M, Alami R and Siciliano B (2021) Physical human-robot interaction with a tethered aerial vehicle: Application to a force-based human guiding problem. *IEEE Transactions on Robotics* 37(3): 723–734.

Xiao M, Liang J, Ji L, Sun Z and Li Z (2022) Aerial photography trajectory-tracking controller design for quadrotor UAV. *Measurement and Control* 55(7-8): 738–745.

Yu Y, Yang S, Wang M, Li C and Li Z (2015) High performance full attitude control of a quadrotor on SO(3). In: *IEEE International Conference on Robotics and Automation (ICRA)*. pp. 1698–1703.

Zhang K, Chermprayong P, Alhinai T, Siddall R and Kovac M (2017) SpiderMAV: Perching and stabilizing micro aerial vehicles with bio-inspired tensile anchoring systems. In: *IEEE/RSJ International Conference on Intelligent Robots and Systems (IROS)*. pp. 6849–6854.

Zheng P, Tan X, Kocer BB, Yang E and Kovac M (2020) TiltDrone: A fully-actuated tilting quadrotor platform. *IEEE Robotics and Automation Letters* 5(4): 6845–6852.

Zufferey R, Tormo-Barbero J, Feliu-Talegón D, Nekoo SR, Acosta JÁ and Ollero A (2022) How ornithopters can perch autonomously on a branch. *Nature Communications* 13(1):

7713.

Supplementary Materials for

A transformable tethered aerial platform for robot-environment interactions

Ruobing Wang, Songnan Bai, Kaixu Dong, Hongqiang Wang, and Pakpong Chirarattananon

S1 Stability analysis for tethered-flight mode with limited position feedback

In the main text, we mentioned that the proposed attitude controller can simultaneously stabilize both the bicopter's attitude and the cable direction around equilibrium, even with limited position feedback. Here, we provide an analysis to support this claim.

To simplify the analysis, we consider the scenario in which position feedback is only available for Bicopter 1, while Bicopter 2 operates with attitude feedback only. The two vehicles are connected by a taut cable, and Bicopter 1's regulated position effectively serves as an inertial reference for Bicopter 2. Below Bicopter 2 is treated as a tethered aerial robot connected to a fixed point.

Under these assumptions, we derive the planar dynamics of the system, where the bicopter operates in the vertical $\boldsymbol{x}$-$\boldsymbol{z}$ plane and the cable extends from the vehicle's attachment point (offset from the CoM) to the fixed reference point. The following notations are (re)defined independently of the main text. We define $\boldsymbol{p} = [p_x, p_z]^\top$ as the position vector of the CoM of the robot, β as the attitude of the robot and ϕ as the angle of the cable. The robot has a mass of m, inertia I, and can generate thrust T and torque τ. The cable attachment point is located at a distance $d > 0$ below the CoM. The cable has a length of l and a tension of f, and its mass and elasticity are negligible. Based on the above definitions, the dynamic equations of the system are derived as:

$$m\ddot{p}_x = T\cos\beta - f\cos\phi, \tag{S1}$$
$$m\ddot{p}_z = -T\sin\beta + f\sin\phi - mg, \tag{S2}$$
$$I\ddot{\beta} = \tau - fd\sin(\beta - \phi). \tag{S3}$$

According to Figure S1, the robot positions p_x and p_z can be expressed with the robot attitude β and the cable angle ϕ as:

$$p_x = d\cos\beta + l\cos\phi, \tag{S4}$$
$$p_z = -d\sin\beta - l\sin\phi. \tag{S5}$$

Substituting (S4) and (S5) into (S1) and (S2) and eliminating the cable tension f with (S3), we can derive the dynamic equations expressed with the robot attitude β and the cable angle ϕ as:

$$\begin{aligned}\ddot{\beta} = &\Big(2\tau - 2d\sin(\beta-\phi)\big(T\cos(\beta-\phi) + mg\sin\phi\big) - 2md\sin(\beta-\phi)\big(d\cos(\beta-\phi)\dot{\beta}^2 + l\dot{\phi}^2\big)\Big) \\ &/\big(2I + d^2m - d^2m\cos(2\beta-2\phi)\big),\end{aligned} \tag{S6}$$

$$\begin{aligned}\ddot{\phi} = 2&\Big(\big((I+md^2)T + m^2gd^2\sin\beta\big)\sin(\beta-\phi) + md\sin(\beta-\phi)\big((I+md^2)\dot{\beta}^2 + mdl\cos(\beta-\phi)\dot{\phi}^2\big) \\ &+ Img\cos\phi - \tau md\cos(\beta-\phi)\Big)/\Big(ml\big(2I + md^2 - md^2\cos(2\beta-2\phi)\big)\Big).\end{aligned} \tag{S7}$$

Defining β_r and ϕ_r as the reference values of the robot attitude and the cable angle, respectively, then based on (S6) and (S7), the reference thrust T_r and torque τ_r in static equilibrium are derived as:

$$T_r = -mg\cos\phi_r\cos(\beta_r - \phi_r), \tag{S8}$$
$$\tau_r = -mgd\cos\beta_r. \tag{S9}$$

Similar to (23), we assume that the robot attitude β is regulated by the a PD controller as:

$$\tau = K_p(\beta_r - \beta) + K_d(\dot{\beta}_r - \dot{\beta}) + \tau_r, \tag{S10}$$

where K_p and K_d are positive scalars representing the control gains. To evaluate the system's stability around the equilibrium, we linearize the dynamic equations (S6) and (S7) for the following equilibrium conditions:

$$\beta = \beta_r, \quad \dot{\beta} = 0, \quad \phi = \phi_r, \quad \dot{\phi} = 0, \quad T = T_r. \tag{S11}$$

This results in the following linear system:

$$\begin{bmatrix}\dot{\beta}\\ \ddot{\beta}\\ \dot{\phi}\\ \ddot{\phi}\end{bmatrix} = \begin{bmatrix}0 & 1 & 0 & 0\\ A_{21} & A_{22} & A_{23} & 0\\ 0 & 0 & 0 & 1\\ A_{41} & A_{42} & A_{43} & 0\end{bmatrix}\begin{bmatrix}\beta-\beta_r\\ \dot{\beta}\\ \phi-\phi_r\\ \dot{\phi}\end{bmatrix}, \tag{S12}$$

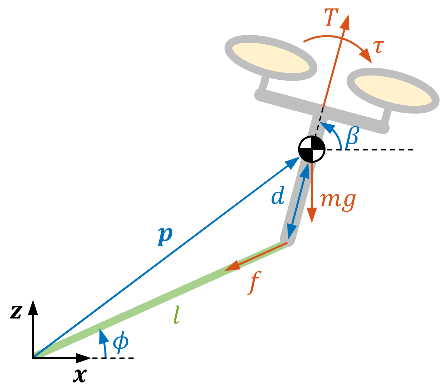

Figure S1. Schematic diagram of a planar tethered aerial robot.

where:

$$A_{21} = \frac{mgd\big(\cos(2\beta_r - 3\phi_r) + 3\cos(2\beta_r - \phi_r)\big)\csc(\beta_r - \phi_r) - 4K_p}{2\big(2I + md^2 - md^2\cos(2\beta_r - 2\phi_r)\big)}, \tag{S13}$$

$$A_{22} = \frac{-2K_d}{2I + md^2 - md^2\cos(2\beta_r - 2\phi_r)}, \tag{S14}$$

$$A_{23} = \frac{-2mgd\cos\beta_r\cot(\beta_r - \phi_r)}{2I + md^2 - md^2\cos(2\beta_r - 2\phi_r)}, \tag{S15}$$

$$A_{41} = \frac{-2Ig\cos\phi_r\cot(\beta_r - \phi_r) + 2d\cos(\beta_r - \phi_r)\big(K_p - mgd\cos\beta_r\cot(\beta_r - \phi_r)\big)}{l\big(2I + md^2 - md^2\cos(2\beta_r - 2\phi_r)\big)}, \tag{S16}$$

$$A_{42} = \frac{2K_d d\cos(\beta_r - \phi_r)}{l\big(2I + md^2 - md^2\cos(2\beta_r - 2\phi_r)\big)}, \tag{S17}$$

$$A_{43} = \frac{2(I + md^2)g\cos\beta_r\csc(\beta_r - \phi_r)}{l\big(2I + md^2 - md^2\cos(2\beta_r - 2\phi_r)\big)}. \tag{S18}$$

Applying the Routh-Hurwitz criterion to the linear system (S12), the requirements for the system to be stable around the equilibrium are obtained as:

$$K_p > -mgd\sin\beta_r, \tag{S19}$$

$$K_p > mgd\big(l\cos(2\beta_r - 3\phi_r) + 3l\cos(2\beta_r - \phi_r) + 4d\cos\beta_r\cos^2(\beta_r - \phi_r)\big)\csc(\beta_r - \phi_r)/(4l). \tag{S20}$$

The conditions (S19) and (S20) indicate that the controller (S10) stabilizes the system around the equilibrium provided that the control gains are sufficiently large. It is noted that the controller (S10) only requires feedback of the robot attitude β, not the cable angle ϕ. This is different from many methods in literature (Lupashin and D'Andrea 2013; Gassner et al. 2017; Tognon et al. 2021) which require external sensors or estimation algorithms to get system states.

Another important condition for the controller (S10) to stabilize the system is that $d > 0$, i.e. the cable attachment point is below the CoM. This also differs from examples in Sanalitro et al. (2020); Dong et al. (2023); Li et al. (2025), which assume that the cable is attached to the CoM. When $d = 0$, then the system in (S12) is marginally stable (with two purely imaginary eigenvalues), regardless of the control gains.

S2 Torque balance condition for quadcopter mode

To obtain the torque balance condition, we consider the net torque about the midpoint of the quadcopter platform P_m in Figure 2(c) and equate it to zero. The forces involved are the weight of the bicopters and the actuation forces $\boldsymbol{f}_{a,i}$ defined by (37). In static equilibrium, $\boldsymbol{f}_{a,i}$ reduces to:

$$\boldsymbol{f}_{a,i} = -m_i\boldsymbol{g} + (-1)^{i-1} f_{r,c}\boldsymbol{u}_c + (-1)^{i-1} f_\tau \boldsymbol{z}_w. \tag{S21}$$

Hence, the condition is:

$$\begin{aligned} &m_1 g\big(d_c\cos(\phi_r - \zeta) - d_m\sin(\phi_r - \zeta)\big) - m_2 g\big(d_c\cos(\phi_r + \zeta) + d_m\sin(\phi_r + \zeta)\big) \\ &- (m_1 g + f_\tau)\big((h_z + d_c)\cos(\phi_r - \zeta) - d_m\sin(\phi_r - \zeta)\big) \\ &+ (m_2 g - f_\tau)\big((h_z + d_c)\cos(\phi_r + \zeta) + d_m\sin(\phi_r + \zeta)\big) = 0, \end{aligned} \tag{S22}$$

in which the first line is attributed to the weight of the bicopters and the subsequent lines are derived from $\boldsymbol{f}_{a,i}$. Note that the terms corresponding to $\boldsymbol{u}_c$ from both bicopters cancel out thanks to the symmetry. Solving for f_τ yields (38).

S3 Conditions for smooth mode transitions

As described in Section 4.3, the proposed platform switches between mode-dependent position controllers to achieve transitions among different modes. To ensure smooth behavior during mode transitions, the reference states for position control in different modes should be designed such that the resulting system positions and geometric states are consistent at the controller switching instants.

S3.1 Free-flight and tethered-flight modes

During the transition between free-flight and tethered-flight modes, the tracking references for position control change from the bicopter positions $\boldsymbol{p}_{r,i}$ to the platform's CoM position $\boldsymbol{p}_{r,c}$ and cable direction ϕ_r and ψ_r. According to the definition of $\boldsymbol{p}_c$ in (6) and the kinematic constraint between the cable and the two bicopters in (7), following conditions should be satisfied:

$$\boldsymbol{p}_{r,c} = \frac{m_1 \boldsymbol{p}_{r,1} + m_2 \boldsymbol{p}_{r,2}}{m_1 + m_2}, \quad \phi_r = \arcsin\left(\frac{\boldsymbol{z}_w^\top (\boldsymbol{p}_{r,1} - \boldsymbol{p}_{r,2})}{\|\boldsymbol{p}_{r,1} - \boldsymbol{p}_{r,2}\|}\right), \quad \psi_r = \arctan\left(\frac{\boldsymbol{y}_w^\top (\boldsymbol{p}_{r,1} - \boldsymbol{p}_{r,2})}{\boldsymbol{x}_w^\top (\boldsymbol{p}_{r,1} - \boldsymbol{p}_{r,2})}\right), \quad \|\boldsymbol{p}_{r,1} - \boldsymbol{p}_{r,2}\| < l_c. \tag{S23}$$

S3.2 Tethered-flight and quadcopter modes

During the transition between tethered-flight and quadcopter modes, the position control continues tracking the reference CoM position $\boldsymbol{p}_{r,c}$, while the control terms related to cable direction ϕ_r and ψ_r are omitted. Since these terms are proportional to the cable length and the cable is short during the transition, their omission has a negligible effect on the system behavior, resulting in a smooth transition.

S4 Stability and robustness analysis for multi-mode flight control

S4.1 Stability of closed-loop dynamics

We analyze the stability of the closed-loop system using the time-scale separation between attitude and translational dynamics, while focusing on the near-equilibrium behavior.

For attitude, we have the following closed-loop dynamics obtained by substituting (23) into (13):

$$\boldsymbol{I}_i \dot{\boldsymbol{\omega}}_i - \boldsymbol{K}_{a,p}\left(\log(\boldsymbol{R}_i^\top \boldsymbol{R}_{r,i})\right)^\vee - \boldsymbol{K}_{a,d}(\boldsymbol{\omega}_{r,i} - \boldsymbol{\omega}_i) = \boldsymbol{\tau}_{f,i} + \boldsymbol{\tau}_{c,i} + \boldsymbol{\tau}_{m,i} - \boldsymbol{\omega}_i \times \boldsymbol{I}_i \boldsymbol{\omega}_i. \tag{S24}$$

Following Yu et al. (2015), local exponential stability holds provided that the feedforward torque $\boldsymbol{\tau}_{f,i}$ sufficiently compensates $\boldsymbol{\tau}_{c,i} + \boldsymbol{\tau}_{m,i}$ and the gyroscopic term $\boldsymbol{\omega}_i \times \boldsymbol{I}_i \boldsymbol{\omega}_i$ remains small, which is reasonable under quasi-static operation.

Since the attitude dynamics are much faster than the translational dynamics for micro aerial robots, we assume that the attitude controller tracks the reference attitudes and thrusts generated by the position controller sufficiently fast. In free-flight mode, substituting (28) into (5) gives the following linear closed-loop dynamics:

$$m_i(\ddot{\boldsymbol{p}}_i - \ddot{\boldsymbol{p}}_{r,i}) + \boldsymbol{K}_{p,p}(\boldsymbol{p}_i - \boldsymbol{p}_{r,i}) + \boldsymbol{K}_{p,d}(\dot{\boldsymbol{p}}_i - \dot{\boldsymbol{p}}_{r,i}) = \boldsymbol{0}, \tag{S25}$$

which yields exponentially stable second-order dynamics. In tethered-flight and quadcopter modes, substituting (31) and (37) into (6) yields:

$$(m_1 + m_2)(\ddot{\boldsymbol{p}}_c - \ddot{\boldsymbol{p}}_{r,c}) + \boldsymbol{K}_{p,p}(\boldsymbol{p}_c - \boldsymbol{p}_{r,c}) + \boldsymbol{K}_{p,d}(\dot{\boldsymbol{p}}_c - \dot{\boldsymbol{p}}_{r,c}) = \boldsymbol{0}, \tag{S26}$$

which has the same exponentially stable second-order error dynamics.

Similarly, for cable direction reguation, substituting (31) into (11) and (12) gives:

$$\frac{m_1 m_2}{m_1 + m_2}\ddot{\phi} + K_{\phi,p}(\phi - \phi_r) + K_{\phi,d}(\dot{\phi} - \dot{\phi}_r) = 0, \tag{S27}$$

$$\frac{m_1 m_2}{m_1 + m_2}\ddot{\psi} + K_{\psi,p}(\psi - \psi_r) + K_{\psi,d}(\dot{\psi} - \dot{\psi}_r) = 0, \tag{S28}$$

which are exponentially stable for slowly varying cable direction references.

S4.2 Robustness to parametric uncertainties and external disturbances

We analyze robustness to parametric uncertainties and external disturbances, focusing on position control as it directly affects task execution and interaction.

S4.2.1 Free-flight mode. Assume that the bicopter mass m_i deviates from the nominal value $\hat{m}_i$ and each bicopter is subject to a constant disturbance force $\boldsymbol{d}_i$. Using $\hat{m}_i$ in (28), adding $\boldsymbol{d}_i$, and substituting the result into (5) yields:

$$m_i(\ddot{\boldsymbol{p}}_i - \ddot{\boldsymbol{p}}_{r,i}) + \boldsymbol{K}_{p,p}(\boldsymbol{p}_i - \boldsymbol{p}_{r,i}) + \boldsymbol{K}_{p,d}(\dot{\boldsymbol{p}}_i - \dot{\boldsymbol{p}}_{r,i}) = (\hat{m}_i - m_i)(\ddot{\boldsymbol{p}}_{r,i} - \boldsymbol{g}) + \boldsymbol{d}_i. \tag{S29}$$

This expression shows that the disturbance induced by mass mismatch scales with the reference acceleration $\ddot{\boldsymbol{p}}_{r,i}$. If the reference varies slowly ($\dot{\boldsymbol{p}}_{r,i} = \ddot{\boldsymbol{p}}_{r,i} = \boldsymbol{0}$), the dynamics reduces to:

$$m_i\ddot{\boldsymbol{p}}_i + \boldsymbol{K}_{p,p}\boldsymbol{p}_i + \boldsymbol{K}_{p,d}\dot{\boldsymbol{p}}_i = \boldsymbol{K}_{p,p}\boldsymbol{p}_{r,i} - (\hat{m}_i - m_i)\boldsymbol{g} + \boldsymbol{d}_i, \tag{S30}$$

which is exponentially stable in the absence of disturbances and exhibits a bounded steady-state error under constant disturbances. The steady-state output is:

$$\boldsymbol{p}_i = \boldsymbol{p}_{r,i} - (\hat{m}_i - m_i)\boldsymbol{K}_{p,p}^{-1}\boldsymbol{g} + \boldsymbol{K}_{p,p}^{-1}\boldsymbol{d}_i. \tag{S31}$$

Hence, the steady-state sensitivities are:

$$\frac{\partial \boldsymbol{p}_i}{\partial m_i} = \boldsymbol{K}_{p,p}^{-1}\boldsymbol{g}, \quad \frac{\partial \boldsymbol{p}_i}{\partial \boldsymbol{d}_i} = \boldsymbol{K}_{p,p}^{-1}. \tag{S32}$$

Therefore, increasing $\boldsymbol{K}_{p,p}$ reduces steady-state sensitivity to both mass uncertainty and external disturbances.

S4.2.2 Tethered-flight mode. We first consider mass uncertainties and external disturbances acting on the platform CoM, and then cable length uncertainty and disturbances acting on the cable direction. Replacing m_i with $\hat{m}_i$ in (31), adding constant disturbances $\boldsymbol{d}_i$, and substituting into (6) yields:

$$(m_1 + m_2)(\ddot{\boldsymbol{p}}_c - \ddot{\boldsymbol{p}}_{r,c}) + \boldsymbol{K}_{p,p}(\boldsymbol{p}_c - \boldsymbol{p}_{r,c}) + \boldsymbol{K}_{p,d}(\dot{\boldsymbol{p}}_c - \dot{\boldsymbol{p}}_{r,c}) = (\hat{m}_1 + \hat{m}_2 - m_1 - m_2)(\ddot{\boldsymbol{p}}_{r,c} - \boldsymbol{g}) + \boldsymbol{d}_1 + \boldsymbol{d}_2. \tag{S33}$$

If $\dot{\boldsymbol{p}}_{r,c} = \ddot{\boldsymbol{p}}_{r,c} = \boldsymbol{0}$, the reduced dynamics is:

$$(m_1 + m_2)\ddot{\boldsymbol{p}}_c + \boldsymbol{K}_{p,p}\boldsymbol{p}_c + \boldsymbol{K}_{p,d}\dot{\boldsymbol{p}}_c = \boldsymbol{K}_{p,p}\boldsymbol{p}_{r,c} - (\hat{m}_1 + \hat{m}_2 - m_1 - m_2)\boldsymbol{g} + \boldsymbol{d}_1 + \boldsymbol{d}_2, \tag{S34}$$

with steady-state CoM position:

$$\boldsymbol{p}_c = \boldsymbol{p}_{r,c} - (\hat{m}_1 + \hat{m}_2 - m_1 - m_2)\boldsymbol{K}_{p,p}^{-1}\boldsymbol{g} + \boldsymbol{K}_{p,p}^{-1}(\boldsymbol{d}_1 + \boldsymbol{d}_2). \tag{S35}$$

The corresponding sensitivities are:

$$\frac{\partial \boldsymbol{p}_c}{\partial m_i} = \boldsymbol{K}_{p,p}^{-1}\boldsymbol{g}, \quad \frac{\partial \boldsymbol{p}_c}{\partial \boldsymbol{d}_i} = \boldsymbol{K}_{p,p}^{-1}. \tag{S36}$$

Similar to the free-flight mode, larger $\boldsymbol{K}_{p,p}$ reduces steady-state sensitivity of the CoM position to mass uncertainty and external disturbances.

Next, replace the cable length l_c with the nominal value $\hat{l}_c$ in (31), include $\boldsymbol{d}_i$, and substitute into (11) and (12) to obtain:

$$\frac{m_1 m_2}{m_1 + m_2}\ddot{\phi} + \frac{\hat{l}_c}{l_c}\big(K_{\phi,p}(\phi - \phi_r) + K_{\phi,d}(\dot{\phi} - \dot{\phi}_r)\big) = \frac{(m_2\boldsymbol{d}_1 - m_1\boldsymbol{d}_2)^\top \boldsymbol{u}_\phi}{(m_1 + m_2)l_c}, \tag{S37}$$

$$\frac{m_1 m_2}{m_1 + m_2}\ddot{\psi} + \frac{\hat{l}_c}{l_c}\big(K_{\psi,p}(\psi - \psi_r) + K_{\psi,d}(\dot{\psi} - \dot{\psi}_r)\big) = \frac{(m_2\boldsymbol{d}_1 - m_1\boldsymbol{d}_2)^\top \boldsymbol{u}_\psi}{(m_1 + m_2)l_c\cos^2\phi}. \tag{S38}$$

The steady-state cable angles are:

$$\phi = \phi_r + \frac{(m_2\boldsymbol{d}_1 - m_1\boldsymbol{d}_2)^\top \boldsymbol{u}_\phi}{K_{\phi,p}(m_1 + m_2)\hat{l}_c}, \tag{S39}$$

$$\psi = \psi_r + \frac{(m_2\boldsymbol{d}_1 - m_1\boldsymbol{d}_2)^\top \boldsymbol{u}_\psi}{K_{\psi,p}(m_1 + m_2)\hat{l}_c\cos^2\phi}. \tag{S40}$$

Therefore, the steady-state sensitivities are:

$$\frac{\partial \phi}{\partial l_c} = 0, \quad \frac{\partial \phi}{\partial \boldsymbol{d}_1} = \frac{m_2\boldsymbol{u}_\phi^\top}{K_{\phi,d}(m_1 + m_2)\hat{l}_c}, \quad \frac{\partial \phi}{\partial \boldsymbol{d}_2} = \frac{-m_1\boldsymbol{u}_\phi^\top}{K_{\phi,d}(m_1 + m_2)\hat{l}_c}, \tag{S41}$$

$$\frac{\partial \psi}{\partial l_c} = 0, \quad \frac{\partial \psi}{\partial \boldsymbol{d}_1} = \frac{m_2\boldsymbol{u}_\psi^\top}{K_{\psi,d}(m_1 + m_2)\hat{l}_c\cos^2\phi}, \quad \frac{\partial \psi}{\partial \boldsymbol{d}_2} = \frac{-m_1\boldsymbol{u}_\psi^\top}{K_{\psi,d}(m_1 + m_2)\hat{l}_c\cos^2\phi}. \tag{S42}$$

Hence, the steady-state cable angles are insensitive to cable length uncertainty, and larger gains $K_{\phi,p}$ and $K_{\psi,p}$ reduce sensitivity to external disturbances. Note that (S42) implies that ψ becomes ill-conditioned as $\phi \to \pm 90^\circ$ due to the azimuth-elevation parameterization; operating near these configurations should be avoided.

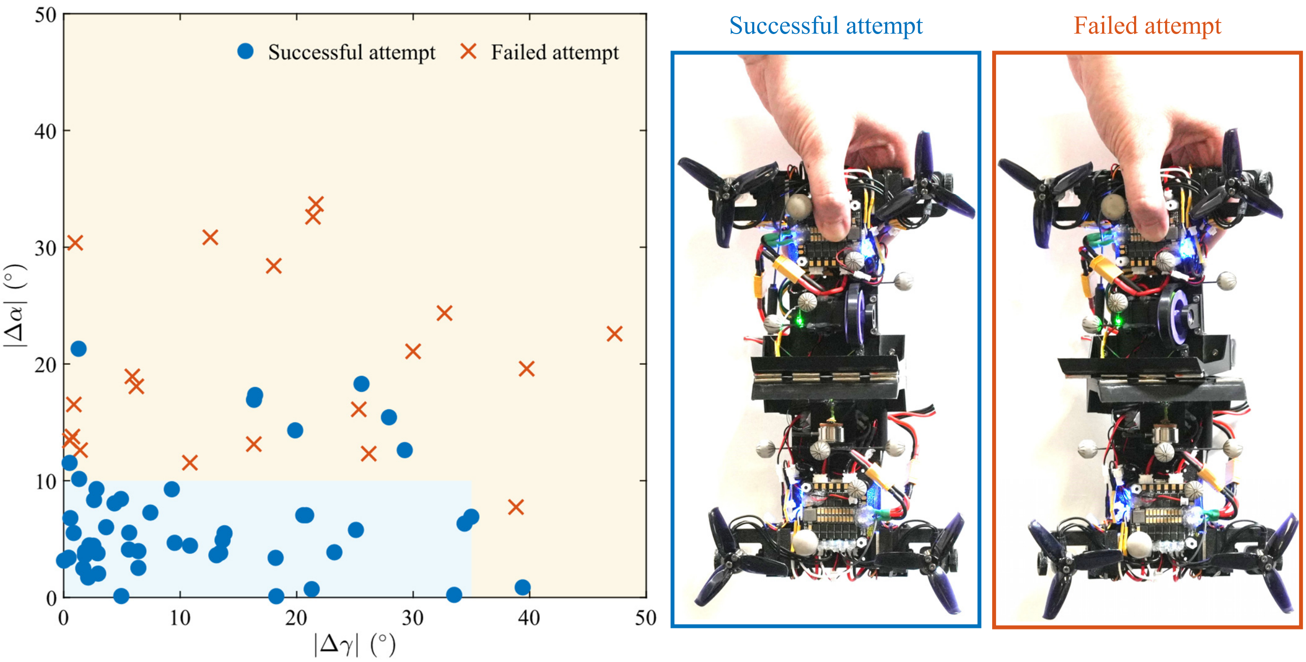

Figure S2. Experimental results (left) and photographs (right) from benchtop tests of the magnetic connection under different attitude misalignment angles.

S4.2.3 Quadcopter mode. Replacing m_i with $\hat{m}_i$ in (37), adding disturbances $\boldsymbol{d}_i$, and substituting into (6) yields the same closed-loop dynamics as (S33). Therefore, the sensitivity results in (S36) also apply, and increasing $\boldsymbol{K}_{p,p}$ reduces the steady-state sensitivity of the CoM position to mass uncertainty and external disturbances.

S5 Misalignment tolerance tests of the magnetic connection

To quantify the mechanical tolerance of the magnetic connection to attitude misalignment, we conducted benchtop tests and measured transition success under different relative orientations. Two bicopters were suspended vertically with Bicopter 1 above Bicopter 2. We manually adjusted the attitude of Bicopter 1 to impose misalignment in the γ_i and α_i directions. Misalignment in β_i was not tested because this rotation was about the magnetic joint axis and did not affect engagement. The winch on Bicopter 1 reeled in the cable from an initial length of $0.15\,\mathrm{m}$ until the bicopters made full contact, emulating the tethered-flight-to-quadcopter transition.

We performed 70 trials with misalignment angles randomly sampled within $\pm 50°$; results were shown in Figure S2. The magnets engaged successfully in 50/70 trials (71.4%). Failures occurred when the misalignment prevented magnetic capture. Within $|\Delta\gamma| < 35°$ and $|\Delta\alpha| < 10°$, all trials succeeded (40/40), which we defined as the effective capture range. These results showed that the magnetic connection tolerated attitude misalignment within a bounded range.